Magma mixing during conduit flow is reflected in melt-inclusion data from persistently degassing volcanoes

Zihan Wei[1], Zhipeng Qin[2], and Jenny Suckale[1]

[1]Stanford University
[2]Guangxi University

March 21, 2023

Abstract

Persistent volcanic activity is thought to be linked to degassing, but volatile transport at depth cannot be observed directly. Instead, we rely on indirect constraints such as CO2-H2O concentrations in melt inclusions trapped at different depth, but this data is rarely straight-forward to interpret. In this study, we develop a multiscale model of conduit flow during passive degassing to identify how flow behavior in the conduit is reflected in melt-inclusion data and surface gas flux. During the approximately steady flow likely characteristic of passive-degassing episodes, variability in degassing arises primarily from two processes, the mixing of volatile-poor and volatile-rich magma and variations in CO2 influx from depth. To quantify how conduit-flow conditions alter mixing efficiency, we first model bidirectional flow in a conduit segment at the scale of tens of meters while fully resolving the ascent dynamics of intermediate-size bubbles at the scale of centimeters. We focus specifically on intermediate-size bubbles, because these are small enough not to generate explosive behavior, but large enough to alter the degree of magma mixing. We then use a system-scale volatile-concentration model to evaluate the joint effect of magma mixing and CO2 influx on volatile concentrations profiles against observations for Stromboli and Mount Erebus. We find that the two processes have distinct observational signatures, suggesting that tracking them jointly could help identify changes in conduit flow and advance our understanding of eruptive regimes.

Magma mixing during conduit flow is reflected in melt-inclusion data from persistently degassing volcanoes

Zihan Wei[1], Zhipeng Qin[2], Jenny Suckale[1]

[1]Department of Geophysics, Stanford University, Stanford, CA, USA
[2]School of Mechanical Engineering, Guangxi University, Nanning, Guangxi, 53004, PR China

Key Points:

- Magma mixing occurs commonly at the interface of up-welling and down-welling magma in persistently degassing volcanoes
- Bubble speed, magma viscosities, bubble volume fraction, and the shear stress at the interface control magma mixing
- Magma mixing and carbon dioxide influx have distinct observational signatures in melt-inclusion data

Corresponding author: Zihan Wei, `zihanwei@stanford.edu`

Abstract

Persistent volcanic activity is thought to be linked to degassing, but volatile transport at depth cannot be observed directly. Instead, we rely on indirect constraints such as CO_2-H_2O concentrations in melt inclusions trapped at different depth, but this data is rarely straight-forward to interpret. In this study, we develop a multiscale model of conduit flow during passive degassing to identify how flow behavior in the conduit is reflected in melt-inclusion data and surface gas flux. During the approximately steady flow likely characteristic of passive-degassing episodes, variability in degassing arises primarily from two processes, the mixing of volatile-poor and volatile-rich magma and variations in CO_2 influx from depth. To quantify how conduit-flow conditions alter mixing efficiency, we first model bidirectional flow in a conduit segment at the scale of tens of meters while fully resolving the ascent dynamics of intermediate-size bubbles at the scale of centimeters. We focus specifically on intermediate-size bubbles, because these are small enough not to generate explosive behavior, but large enough to alter the degree of magma mixing. We then use a system-scale volatile-concentration model to evaluate the joint effect of magma mixing and CO_2 influx on volatile concentrations profiles against observations for Stromboli and Mount Erebus. We find that the two processes have distinct observational signatures, suggesting that tracking them jointly could help identify changes in conduit flow and advance our understanding of eruptive regimes.

Plain Language Summary

Some volcanoes like Stromboli or Mount Erebus, named persistently degassing volcanoes, erupt multiple times a day, emitting copious gas and thermal energy with little magma. Direct measurements of these volcanoes provide rich datasets for understanding how these volcanic systems work. Without the ability to observe processes at depth before magma reaches the surface, we rely on erupted samples to interpret these processes. Some of these samples seal magma droplets named melt inclusions during ascent, which thus represent valuable snapshots of magma composition. Here we study how the magma flow in the conduit connecting the surface to the source of magma contribute to the compositions of melt inclusions using numerical simulations. We demonstrate that the gas-rich, up-welling magma will mixing with the down-welling magma, which loses its gas at the surface. The degree of mixing depends on the physical properties of magma and gas bubbles. This magma mixing, together with the influx of carbon dioxide into the system, significantly shift the concentrations of water and carbon dioxide in melt inclusions. Our study shows that magma mixing is almost inevitable in persistently degassing volcanoes. We suggest that melt inclusion data could potentially help us track the evolving flow conditions in volcanic conduits.

1 Introduction

Not all volcanic activity is rare: Persistently degassing volcanoes like Stromboli, Italy, or Mount Erebus, Antarctica, typically erupt multiple times a day (Dibble et al., 1988; Burton, Allard, et al., 2007). While eruptions are frequent, they are mild by volcanic standards and can be monitored directly, providing rich datasets for constraining how these volcanic systems work (Burton, Allard, et al., 2007; Oppenheimer et al., 2009; Johnson et al., 2008; Ilanko et al., 2015; Ripepe et al., 2015).

Measurements of surface gas fluxes show that persistently degassing volcanoes continually emit copious quantities of gas and thermal energy, but rarely erupt magma (Stoiber & Williams, 1986; Allard et al., 1994; Kazahaya et al., 1994; Palma et al., 2008; Oppenheimer et al., 2009; Woitischek et al., 2020). This imbalance suggests that more magma is being degassed than erupted, which leads to bidirectional flow of volatile-rich, less viscous magma ascending in the center of the conduit and volatile-poor, more viscous magma descending along the sides (Francis et al., 1993; Kazahaya et al., 1994; Stevenson & Blake, 1998).

The concept of bidirectional flow is appealing from a theoretical point of view, because it provides the significant thermal energy flux required to maintain open-system conditions in persistently degassing volcanoes. Evaluating it from an observational point of view, has proven more challenging. One exception is the 1959 eruption at Kīlauea Iki, Hawaii, where recent work suggests that the predominance of certain misalignment angles in olivine glomerocrysts emerges naturally only when the pre-eruptive conduit flow field was bidirectional (DiBenedetto et al., 2020). However, the majority of degassing observations refer to non-eruptive conditions (e.g., Burton, Allard, et al., 2007; Oppenheimer et al., 2009; Ruth et al., 2018), emphasizing the need to link flow conditions and degassing processes during approximately steady conditions.

Some erupted samples can be used to reconstruct the degassing processes prior to eruption, because they contain host crystals that have entrapped small droplets of melts during their growth (e.g., Métrich et al., 2001, 2010; Oppenheimer et al., 2011; Rasmussen et al., 2017). These melt inclusions are sealed in at various depth and thus represent valuable snapshots of evolving melt compositions (Ruth et al., 2018). Patching together these snapshots to obtain a consistent picture of degassing at depth, however, is hindered by the limited fidelity with which melt-inclusion seal in pre-eruptive conditions at depth (Bucholz et al., 2013; Aster et al., 2016; Barth et al., 2019) and measurement uncertainty (Oppenheimer et al., 2011). Another important observable that helps to constrain steady degassing is the surface-gas flux (Burton, Allard, et al., 2007; Oppenheimer et al., 2009; Ilanko et al., 2015). Surface gas flux measurements provide an important complement to melt inclusion data, because melt inclusions only seal melt and are unsuitable for estimating the total budgets of volatiles with low solubility, such as CO_2 (e.g., Wallace, 2005; Burton, Mader, & Polacci, 2007)

The goal of this study is to quantify how different rates of magma mixing during conduit flow and variations in CO_2 influx alter the volatile concentrations recorded by melt-inclusions during passive degassing. We hypothesize that CO_2 influx (Burton, Mader, & Polacci, 2007; Blundy et al., 2010; Métrich et al., 2010; Rasmussen et al., 2017) and magma mixing (Witham, 2011a; Moussallam et al., 2016) leave distinct observational signatures in melt-inclusion data. Identifying these distinct observational signatures would allow distinguishing between the relative importance of the two processes during conduit flow and potentially afford new insights into their relationship with eruptive behavior. Spilliaert et al. (2006) provide a proof-of-concept of this idea, but without linking in a magma dynamics model.

To connect conduit flow to melt-inclusion data, we link a multiscale model of bidirectional conduit flow to a volatile-concentration model. The conduit-flow model is multiscale in the sense that it resolves both the flow dynamics of a conduit segment at the tens-of-meter scale and the ascent dynamics of centimeter-scale bubbles through a direct numerical approach (Qin & Suckale, 2017; Suckale et al., 2018; Qin et al., 2020). We focus on resolving intermediate-size bubbles at the scale of centimeters that are buoyant enough to decouple from the magmatic liquid and ascend, but not so large that they might be related to eruptive behavior (e.g., Jaupart & Vergniolle, 1988). Smaller crystals and or bubbles at the millimeter scale have much smaller ascent speeds and hence remain largely entrained (Tryggvason et al., 2013). As a consequence, their main effect is to alter the effective material properties of the bubble-crystal-melt mixture (Bowen, 1976).

We test our hypothesis by comparing model results against the volatile concentrations recorded in melt inclusions. We first quantify magma mixing with the conduit-flow model and then use the volatile-concentration model based on Witham (2011a) to calculate the associated system-scale concentration profiles. We focus specifically on Stromboli and Mount Erebus, because of their abundance of melt inclusion data (Métrich et al., 2010; Oppenheimer et al., 2011; Rasmussen et al., 2017), the availability of continuous measurements of surface gas fluxes (Burton, Allard, et al., 2007; Oppenheimer et al., 2009; Ilanko et al., 2015), and the relatively steady patterns of their degassing and eruption activities (Allard et al., 1994; Burton, Allard, et al., 2007; Oppenheimer et al., 2009; Métrich et al., 2010; Oppenheimer et al., 2011; Rasmussen et al., 2017).

A particularly puzzling observation is that melt inclusions from many persistently degassing volcanoes consistently indicate higher CO_2 content than predicted by either closed-system or open-system degassing path (Métrich & Wallace, 2008; Métrich et al., 2010; Blundy et al., 2010; Oppenheimer et al., 2011; Yoshimura, 2015; Rasmussen et al., 2017; Barth et al., 2019). In contrast, melt inclusions from more silicic volcanoes appear to match the expected trends more closely (e.g., Schmitt, 2001; Liu et al., 2006), suggesting that melt inclusions may at least partially reflect systematic differences in conduit flow between different volcanic systems. While CO_2 influx (Burton, Mader, & Polacci, 2007; Shinohara, 2008; Blundy et al., 2010; Métrich et al., 2010; Rasmussen et al., 2017) and magma mixing (Dixon et al., 1991; Witham, 2011a; Sides et al., 2014) are often presented as alternative explanations (Métrich et al., 2011; Witham, 2011b), we argue here that they both contribute to the observed variability in volatile concentrations, but do so in distinct ways.

2 Method

From individual bubbles and crystals to transcrustal plumbing systems (Cashman et al., 2017), volcanic systems bridge ten orders of magnitude in spatial scales or more (e.g., fig. 1). Fully resolving all physical and chemical processes over this vast spectrum of spatial scales at the accuracy necessary to understand the nonlinear dynamics of a highly coupled system is not possible. Instead, we develop a customized multiscale model that focuses on the key elements required for linking bidirectional conduit flow and observations of melt-inclusions and surface-gas flux. Our model consists of two main components, the conduit-flow model and the volatile-concentration model, described in more detail in the next two sections.

2.1 Conduit-flow Model

Transcrustal plumbing system (Cashman et al., 2017; Magee et al., 2018) consists of vertically stacked melt-rich tabular lenses and vertical conduit-like segments transiently connecting these lenses (see fig. 1D). While magma properties, such as gas volume fraction and melt viscosity, can vary significantly over the entirety of this system, we assume that they are approximately constant at the scale of the vertical, conduit-like segments (fig. 1C). This assumption implies that exsolution and dissolution are negligible within the segments. Volatiles exsolved at depth provide the buoyancy required for the ascent of volatile-rich magma. Upon degassing at the free surface, volatile-poor magma remains and sinks back to depth, creating a bidirectional flow field (Blake & Campbell, 1986; Francis et al., 1993; Kazahaya et al., 1994; Stevenson & Blake, 1998; Molina et al., 2012). More specifically, we assume core-annular flow here, because this particular bidirectional flow field is most commonly observed in vertical pipes at moderate to high viscosity contrasts (Stevenson & Blake, 1998; Beckett et al., 2011; Suckale et al., 2018).

In the conduit segments, centimeter-scale gas bubbles segregate from the ambient magma flow and rise towards the surface to degas. We capture these bubbles explicitly using direct numerical simulations (fig. 1B). Crystals and millimeter-scale bubbles, however, have much smaller segregation speeds and hence largely remain entrained in the ambient magma flow. We represent these implicitly through a mixture approximation (Bowen, 1976) by reducing their effect to changes in the effective density and viscosity of the crystal- and bubble-bearing magma (fig. 1A). For the rest of this manuscript, we

Table 1. Definition of symbols

$\rho(kg/m^3)$: magma density
$\mu(kg/m^3)$: magma viscosity
$\rho_c(kg/m^3)$: density of volatile-rich magma
$\rho_a(kg/m^3)$: density of volatile-poor magma
$\rho_b(kg/m^3)$: density of bubbles
$M_b(kg)$: mass of a bubble
$\mathbf{F}_b(N)$: hydrodynamic force exerted onto the bubble by the surrounding magma
$\mathbf{X}_b(m)$: bubble location
$\mu_c(Pa \cdot s)$: viscosity of volatile-rich magma
$\mu_a(Pa \cdot s)$: viscosity of volatile-poor magma
$\mathcal{S}$: speed ratio
$\mathcal{I}$: interface stability number
Γ(%/MPa): mixing factor
σ(%/MPa): error of mixing factor
$R(m)$: conduit radius
$L(m)$: conduit length
$r(m)$: bubble radius
ϕ: volume fraction of resolved bubbles in volatile-rich magma
ϕ_{tot}: total volume fraction of resolved and subgrid bubbles in volatile-rich magma
c: concentration variable in conduit-flow simulations
$D(m^2/s)$: diffusion coefficient
i_u: weight percent of dissolved volatiles in up-welling magma
i_d: weight percent of dissolved volatiles in down-welling magma
i_g: weight percent of exsolved volatiles in up-welling magma
i_*: effective up-welling volatile content
$p(Pa)$: pressure in the conduit-flow model
$P(Pa)$: pressure in the calculation of volatile concentration profiles
$\Delta p(Pa)$: pressure step size
$P_{min}(Pa)$: minimum pressure in the calculation of volatile concentration profiles
$P_{max}(Pa)$: maximum pressure in the calculation of volatile concentration profiles
$\mathbf{v}(m/s)$: velocity
$\mathbf{V}_b(m/s)$: bubble velocity
$U(m/s)$: characteristic speed of the analytical solution of core-annular flow
$v_c(m/s)$: vertical speed at the center line of the analytical solution
$v_b(m/s)$: analytical bubble rise speed
$\tau_{xy}(Pa)$: simulated shear stress
$\tau(Pa)$: analytical interfacial shear stress
t: nondimensional time
$g(m/s^2)$: gravitational acceleration
λ: H_2O/CO_2 in the gas phase at the surface

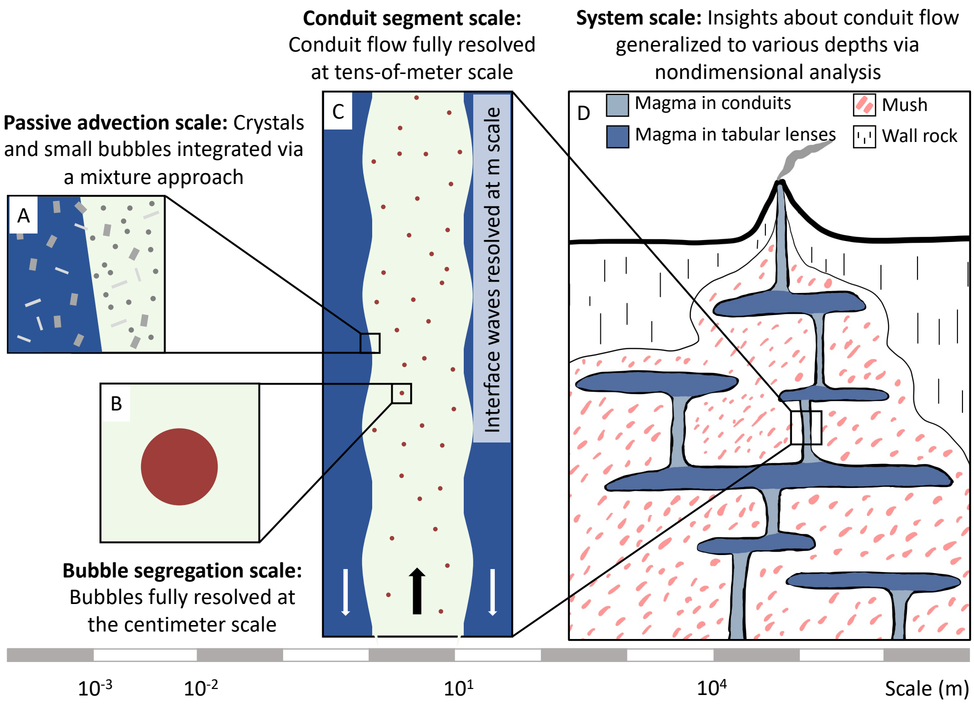

Figure 1. Overview of relevant spatial scales and their model representation.

use the term "magma" to refer to the mixture of melt and passively advected crystals and bubbles. Resolving actively segregating bubbles while incorporating passively advecting bubbles and crystals through a subgrid mixture model is commonly used in multiphase modeling as reviewed in Tryggvason et al. (2013).

The first step of our analysis is to quantify magma mixing via the multiscale conduit-flow model (fig. 2). The multiscale approach described above reduces our model to three distinct phases, the volatile-rich, up-welling magma, the volatile-poor, down-welling magma and gas bubbles of intermediate size, contained mostly in the up-welling flow. All model variables and parameter choices are summarized in table 2. The viscosities for both magmas in our model are informed by previously estimated ranges for Stromboli (Burton, Mader, & Polacci, 2007) and Mount Erebus(Sweeney et al., 2008). Since our model focuses on approximately steady flow during non-eruptive phases, we do not consider the potential presence of large bubbles or slugs, because these are related to eruptive processes (Jaupart & Vergniolle, 1988; Del Bello et al., 2012; Qin et al., 2018). Since our bubbles are not large enough to deform significantly, we model them as spherical in the interest of simplicity.

We define a 2D rectangular simulation domain (fig. 2A) to represent a conduit segment (fig. 1C). We apply a stress-free condition ($p = const.$, $\frac{\partial \mathbf{v}}{\partial x} = 0$) at the top boundary to enable free outflow. At the base we impose the analytical solution of vertical speed in core-annular flow (Suckale et al., 2018). The side walls are no-slip. We assume that the two magmas are miscible Newtonian fluids differing in density and viscosity. The volatile-rich magma has lower density because the entrained small bubbles reduce the effective density of magma (fig. 1). The volatile-rich magma is less viscous by 1 to 2 orders of magnitude because it contains higher concentration of dissolved H_2O and lower amount of crystals (e.g., McBirney & Murase, 1984; Giordano et al., 2008).

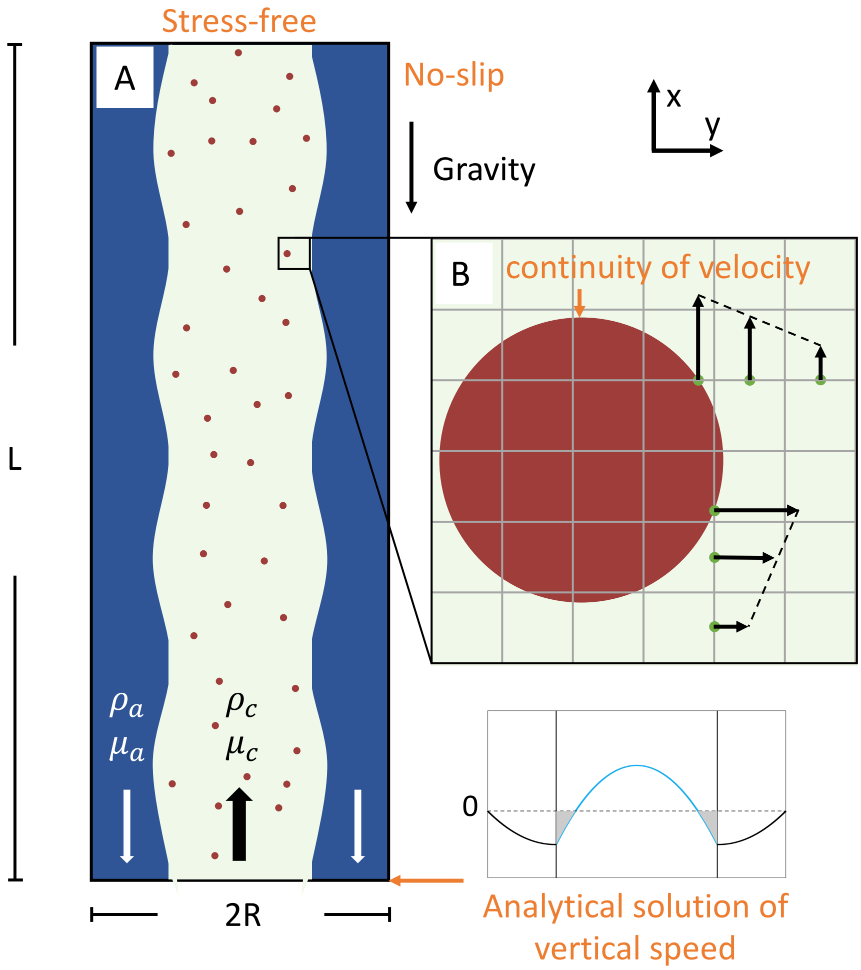

Figure 2. Illustration of the simulation domain (not to scale). The orange text represents the boundary conditions. **(A)**: The model domain for simulating the conduit flow. In this study, L =21m and R =1.5m. **(B)**: We enforce the continuity of velocity as the boundary condition at the bubble-magma interface by linearly interpolating the bubble velocity and magma velocity for magma grid cells adjacent to bubbles, see Qin and Suckale (2017) for details. Vertical and horizontal arrows represent vertical and horizontal velocity components, respectively. Figure (B) modified from Qin and Suckale (2017).

Our model solves for the mass and momentum balance in an incompressible core-annular flow at low Reynolds number (Qin & Suckale, 2017; Suckale et al., 2018; Qin et al., 2020). The governing equations are conservation of mass and momentum

$$0 = -\nabla p + \nabla \cdot (\mu \nabla \mathbf{v}) + \rho \mathbf{g}, \tag{1}$$

and advection-diffusion equation for concentration to capture magma mixing

$$\frac{\partial c}{\partial t} + \mathbf{v} \cdot \nabla c = D \nabla^2 c, \tag{2}$$

where density, ρ, and viscosity, μ, are defined as

$$\rho = \begin{cases} \rho_a - c(\rho_a - \rho_c), & \text{in magma} \\ \rho_b, & \text{in bubbles} \end{cases}, \tag{3}$$

$$\mu = \mu_a - c(\mu_a - \mu_c), \tag{4}$$

p is pressure, $\mathbf{v}$ is velocity, and g is the gravitational acceleration. We solve the flow field on a Cartesian staggered grid with the finite difference method as described in detail by Qin and Suckale (2017). The concentration variable, c, in eq. 2 represents the content of dissolved volatile and subgrid bubbles and ranges from $c \in [0, 1]$. The diffusion coefficient $D = 10^{-10}\mathrm{m}^2/\mathrm{s}$ refers to the diffusion of water in basaltic magma (Zhang & Stolper, 1991; Witham, 2011a). Initially, $c = 1$ in the volatile-rich magma and $c = 0$ in the volatile-poor magma. For the purpose of analyzing the flow regime stability, we define the contour of $c = 0.5$ as the interface between the two magmas. We assume that the density and viscosity of magma depend linearly on c, as shown in eqs. 3 and 4, where $\rho_c, \rho_a, \mu_c, \mu_a$ are the density and viscosity of the volatile-rich and volatile-poor magmas, respectively.

Following Qin and Suckale (2017), Qin et al. (2020), and Qin and Suckale (2020), we describe intermediate-size bubbles by the Newton's Laws of Motion

$$M_b \frac{d\mathbf{V}_b}{dt} = \mathbf{F}_b + M_b \mathbf{g}, \tag{5}$$

$$\frac{d\mathbf{X}_b}{dt} = \mathbf{V}_b, \tag{6}$$

where M_b is the mass of a bubble, $\mathbf{V}_b$ the bubble velocity, $\mathbf{F}_b$ the hydrodynamic force exerted onto the bubble by the surrounding magma, and $\mathbf{X}_b$ the bubble location. As shown in fig. 2B, we enforce continuity of velocity at the bubble-magma interface by linearly interpolating the bubble velocity and magma velocity for magma grid cells adjacent to bubbles.

The numerical implementation (Wei et al., 2021) consists of three steps. The first step is solving eq. 1. In this step, we modify the numerical implementation of Qin and Suckale (2017), Qin et al. (2020), and Qin and Suckale (2020) by using the actual density of each phase to reduce the convergence steps. These previous studies use liquid density for the entire domain in the scenario where different phases have similar densities, which is inconsistent with this study. The second step is solving eq. 2 following Suckale et al. (2018). The third step is solving bubble motion following Qin and Suckale (2017), Qin et al. (2020), and Qin and Suckale (2020).

In our model setup, magma mixing occurs at the interface (fig. 2A) between volatile-rich and volatile-poor magma. Previous studies demonstrate that in the absence of small bubbles or crystals in the flow, the interface is stable for two miscible magmas with low diffusivity, D (Stevenson & Blake, 1998; Suckale et al., 2018). The presence of bubbles and crystals, however, might lead to significantly more mixing than observed in the purely fluid limit, because interactions between both bubbles and crystals act over a very long spatial range at low Reynolds number (Segre et al., 1997). Even at very low phase fractions of a few percent of solids or bubbles in the flow, multiphase interactions create spatial correlations in velocity that are reminiscent of turbulence at high Reynolds number (Xue et al., 1992; Tong & Ackerson, 1998; Levine et al., 1998). In volcanic systems, mixing is hence dominated by multiphase processes rather than turbulence. In that aspect, our model differs from Witham (2011a), who assumed turbulent mixing.

To quantify the magma mixing that occurs at the scale of a conduit segment, we define the mixing factor Γ as the mixing associated with a pressure drop of $\Delta p = 1\mathrm{MPa}$. We calculate Γ from the concentration in the magma entering the domain from the bottom (c_b) and leaving the domain from the top (c_t) by averaging c in the up-welling magma laterally. We use the median value of $\frac{c_b - c_t}{c_b}$ over time as the estimated amount of mixing after the up-welling magma moves through the domain. The pressure drop in this process is $\frac{L(\rho_a+\rho_c)g}{2}$. For each conduit flow simulation, we compute Γ and its associated error σ as

$$\begin{Bmatrix}\Gamma \\ \sigma\end{Bmatrix} = 1 - \left[1 - \begin{Bmatrix} median \\ std \end{Bmatrix} \left(\frac{c_b - c_t}{c_b}\right)\right]^{\frac{2\Delta p}{L(\rho_a+\rho_c)g}}. \tag{7}$$

2.2 Volatile-concentration Model

As a consequence of mixing, the up-welling magma is gradually diluted as it ascends, while the down-welling magma becomes more volatile-rich as it descends. Using the estimated mixing factors from our simulations, we compute CO_2-H_2O concentration profiles at a system scale following Witham (2011a) with some modifications (Wei et al., 2021). For both CO_2 and H_2O, we calculate the steady-state concentration profiles i_u, i_d and i_g that represent the weight percent of dissolved volatiles in the up-welling magma, dissolved volatiles in the down-welling magma, and exsolved, up-welling volatiles, respectively. Although some bubbles enter the down-welling magma in our simulations, most of these bubbles return to the up-welling magma relatively quickly or continue ascending in down-welling magma because of their own buoyancy (fig. 4G), introducing only a minor and transient disruption. Therefore, we assume that no exsolved volatiles descend.

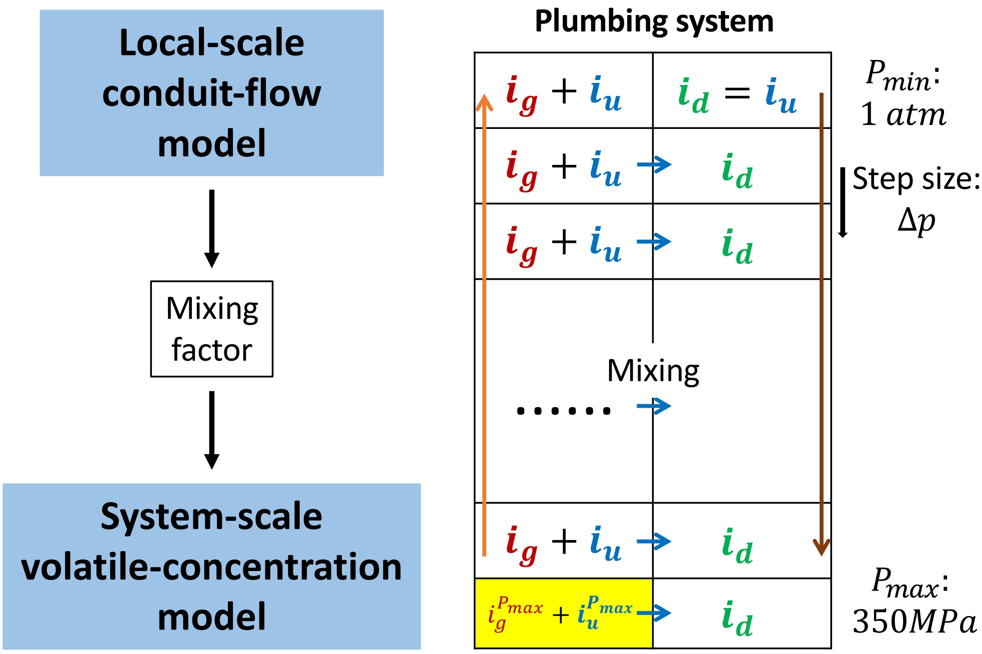

Figure 3. Left: workflow of our analysis. We summarize the simulation result of the conduit-flow model as a mixing factor, which is an input parameter for the system-scale volatile-concentration model. Right: Illustration of the volatile-concentration model. The yellow cell represents the fixed input set as the composition of the most volatile-rich melt inclusions.

We illustrate the calculation of CO_2-H_2O concentration profiles in fig. 3. The pressure P ranges from $P_{min} = 0.1$ MPa to P_{max} with a step size Δp. We set $i_u^{P_{max}} + i_g^{P_{max}}$ as the composition of the most volatile-rich melt inclusions (Métrich et al., 2010; Oppenheimer et al., 2011), and set $P_{max} = 350$MPa based on the volatile solubility model MagmaSat (Gualda et al., 2012; Ghiorso & Gualda, 2015). We assume a constant magma temperature 1180°C and 1000°C for Stromboli (Bertagnini et al., 2003; Métrich et al., 2010) and Mount Erebus (Kyle, 1977), respectively.

Following Witham (2011a), we initialize i_u and i_g according to closed-system degassing. Then, we initialize the down-welling concentration profile by calculating

$$i_d^P = (1-\Gamma)\, i_d^{P-\Delta p} + \Gamma i_u^P \tag{8}$$

for the entire pressure range. The superscripts indicate the pressure corresponding to the concentrations. We assume $i_d^{P_{min}} = i_u^{P_{min}}$, because up-welling magma starts to sink at the surface. Witham (2011a) defines the effective up-welling concentration i_*^p as

$$\phi_u i_*^P = \phi_u \left(i_u^P + i_g^P\right) - \phi_d i_d^P, \tag{9}$$

where ϕ_u and ϕ_d are the up-welling and down-welling mass flux, respectively. We assume negligible magma extrusion and approximately steady degassing such that $\phi_u = \phi_d$ and i_* is constant throughout the domain, yielding

$$i_* = i_u^P + i_g^P - i_d^P. \tag{10}$$

Once i_* is known, we can compute $i_u + i_g$ at each depth using eq. 10 and i_d. We then update i_u and i_g by partitioning i_u^P and i_g^P for the entire pressure range using MagmaSat (Gualda et al., 2012; Ghiorso & Gualda, 2015).

To compute i_*, we fix $i_u^{P_{max}} + i_g^{P_{max}}$, rather than fix $i_g^{P_{min}}$ as Witham (2011a) does. We can also vary $i_u^{P_{max}} + i_g^{P_{max}}$ to test the effect of variable volatile influx. We make this adjustment because current measurements only constrain surface gas flux (Burton, Allard, et al., 2007; Oppenheimer et al., 2009). Using surface gas flux to compute $i_g^{P_{min}}$ requires the knowledge of ϕ_u, which is unavailable from data. We hence compute i_* by

$$i_* = i_u^{P_{max}} + i_g^{P_{max}} - i_d^{P_{max}}. \tag{11}$$

After updating i_u and i_g, we iterate eqs.(8), (11), and (10) until reaching a steady state.

3 Results

3.1 Bubbles Can Lead to Substantial Magma Mixing in Volcanic Conduits

To understand how intermediate-size gas bubbles create magma mixing during bidirectional conduit flow, we perform a series of simulations summarized in Table 2 with selected snapshots shown in fig. 4. We find that bubble speed (figs. 4A-C), the viscosities of both magmas (figs. 4A and D), and the volume fraction of resolved bubbles control the stability of the flow regime. The resolved bubbles, together with the subgrid bubbles contributing to the density difference between the volatile-rich and volatile-poor magma, correspond to total bubble fractions ranged from 2.1% to 12.0% in our simulations (table 2). To account for the different flow speeds in the simulations, we compare them at the same non-dimensional time t. We use R as the characteristic length and the vertical speed at the center line, v_c, of the analytical solution enforced at the bottom boundary as the characteristic speed in our nondimensionalization (Suckale et al., 2018).

For constant magma properties, bubble speed depends on both bubble radius and bubble density. Using fig. 4A as the baseline, we reduce the bubble size by 30% in simulation No. 2 shown in fig. 4B and reduce the density contrast between bubble and up-welling magma by 49% in simulation No. 3 shown in fig. 4C. All other parameters are constant. We select these particular values, including the unrealistically high bubble density in simulation No. 3, to keep the analytical bubble rise speed $v_b = (\rho_c - \rho_b)gr^2/\mu_c$

Table 2. Values of variables in simulations.

Simulation No.	$\rho_c(kg/m^3)$	$\rho_a(kg/m^3)$	$\rho_b(kg/m^3)$	$\mu_c(Pa \cdot s)$	$\mu_a(Pa \cdot s)$	$r(m)$	ϕ	ϕ_{tot}	$\mathcal{S}$	$\mathcal{I}$	Γ(%/MPa)	σ(%/MPa)
1	2400	2500	600	3×10^4	9×10^4	4.3×10^{-2}	2%	7.16%	4.05×10^{-1}	7.36×10^{-8}	10.16	19.09
2	2400	2500	600	3×10^4	9×10^4	3×10^{-2}	2%	7.16%	2.83×10^{-1}	7.36×10^{-8}	2.97	2.97
3	2400	2500	1518	3×10^4	9×10^4	4.3×10^{-2}	2%	11.98%	2.29×10^{-1}	5.51×10^{-8}	2.93	3.90
4	2400	2500	600	1.85×10^4	5.55×10^4	4.3×10^{-2}	2%	7.16%	4.05×10^{-1}	1.94×10^{-7}	22.55	38.07
5	2400	2500	76.21	5×10^4	1.5×10^5	4.3×10^{-2}	2%	6.04%	4.85×10^{-1}	3.07×10^{-8}	5.57	3.43
6	2450	2452	300	6×10^3	1.8×10^4	4.3×10^{-2}	2%	2.09%	1.46×10^0	2.01×10^{-7}	82.07	23.07
7	2400	2500	600	2×10^4	2×10^5	4.3×10^{-2}	2%	7.16%	7.90×10^{-1}	3.33×10^{-8}	3.34	5.32
8	2400	2500	600	9×10^3	9×10^4	4.3×10^4	2%	7.16%	7.90×10^{-1}	1.65×10^{-7}	13.00	13.26
9	2400	2500	600	9×10^3	9×10^4	6×10^{-2}	2%	7.16%	1.11×10^0	1.65×10^{-7}	34.41	26.79
10	2450	2452	300	5×10^3	5×10^4	4.3×10^{-2}	2%	2.09%	2.85×10^0	5.84×10^{-8}	84.34	28.8
12	2400	2500	600	5×10^3	5×10^5	6×10^{-2}	2%	7.16%	7.77×10^0	9.55×10^{-9}	3.26	30.67
11	2400	2500	600	2×10^4	1×10^6	4.3×10^{-2}	2%	7.16%	2.91×10^0	2.21×10^{-9}	0.54	3.15
13	2400	2500	600	3×10^4	9×10^4	4.3×10^{-2}	1%	6.21%	2.33×10^{-1}	2.77×10^{-8}	3.57	7.41
14	2400	2500	600	3×10^4	9×10^4	4.3×10^{-2}	3%	8.11%	5.36×10^{-1}	1.42×10^{-7}	19.31	27.87
15	2400	2500	600	9×10^3	9×10^4	6×10^{-2}	1.5%	6.68%	8.88×10^{-1}	1.08×10^{-7}	17.60	10.44
16	2400	2500	700	5×10^3	2.5×10^5	6×10^{-2}	0.5%	6.03%	1.20×10^0	5.61×10^{-9}	0.17	0.70
17	2400	2500	300	3×10^4	3×10^5	4.3×10^{-2}	1%	5.50%	5.18×10^{-1}	5.87×10^{-9}	0.06	0.07
18	2520	2550	100	5×10^3	1×10^5	6×10^{-2}	1.3%	2.80%	3.58×10^0	2.37×10^{-8}	57.88	42.80
19	2450	2550	300	8×10^3	1.6×10^5	6×10^{-2}	1.5%	6.36%	1.70×10^0	4.94×10^{-8}	7.13	24.74
20	2366	2500	-	5×10^3	2.5×10^5	-	0%	7.44%	0	0	0.13	0.08
Example magma properties at deep and shallow conduit:												
Deep	2400	2500	700	5×10^3	2.5×10^5	1×10^{-2}	0.5%	6.03%	2.01×10^{-1}	5.61×10^{-9}		
Shallow	2400	2500	100	2×10^4	1×10^5	8×10^{-2}	3%	7.04%	1.49×10^0	2.02×10^{-7}		

the same in both simulations, so that the bubble speed is approximately the same. Here ρ_b is the bubble density, r the bubble radius, and μ_c the viscosity of the volatile-rich magma.

Fig. 4A shows a flow field with significant mixing (Γ=10.16%). The oscillatory interface separating the two magmas entraps some of the volatile-poor magma into the volatile-rich magma. In contrast, both figs. 4B and C show a flow field with a much smaller and similar degree of mixing (Γ=2.97% and 2.93%, respectively) and a stabler core-annular geometry. As compared to fig. 4A, the entrapment of volatile-poor magma into the volatile-rich magma is less frequent and entails smaller batches of magma.

Figs. 4A and D highlight the importance of both magma viscosities, μ_c and μ_a in governing mixing. With both viscosities equally increased by $\frac{2}{3}$, the flow field in fig. 4D becomes more stable and exhibits less mixing (Γ=5.57%) than in fig. 4A. In addition to increasing both magma viscosities, we decrease bubble density in fig. 4D to ensure that the bubble speed is the same in both simulations. We maintain a constant viscosity contrast between the magmas to isolate the effect of individual magma viscosities from that of a varying viscosity contrast, which also affects the bidirectional flow regime (Stevenson & Blake, 1998).

Figs. 4A and E highlight the importance of the volume fraction of centimeter-scale bubbles. With the resolved bubble volume fraction increased to 3%, the flow field in fig. 4E becomes less stable and exhibits more mixing (Γ=19.31%) than in fig. 4A. Comparing simulation No. 1 with 13 and 9 with 15 also demonstrates that decreasing the resolved bubble volume fraction decreases the degree of mixing (see table 2).

Fig. 4F illustrates the compound effect of increasing bubble speed and decreasing magma viscosities. In this simulation, v_b is 6 times higher than in fig. 4A and the magma viscosities are a fifth of those in fig. 4A. The consequence is extensive mixing and a complete collapse of core-annular flow. It may seem surprising that bubbles with radii much smaller than the conduit width can have such a profound effect on conduit flow at bubble fractions as low as 2%. To understand the physical mechanism, we quantify the stress disruptions created by bubbles stirring the bidirectional interface (fig. 5). Fig. 5A shows the interfacial stress deviation, $\tau_{xy} - \tau$, where τ_{xy} is the simulated shear stress and τ is the analytical interfacial shear stress (Suckale et al., 2018). The interfacial stress deviations lead to localized interface deformation, and, if pronounced enough, to interfacial wave build-up and mixing.

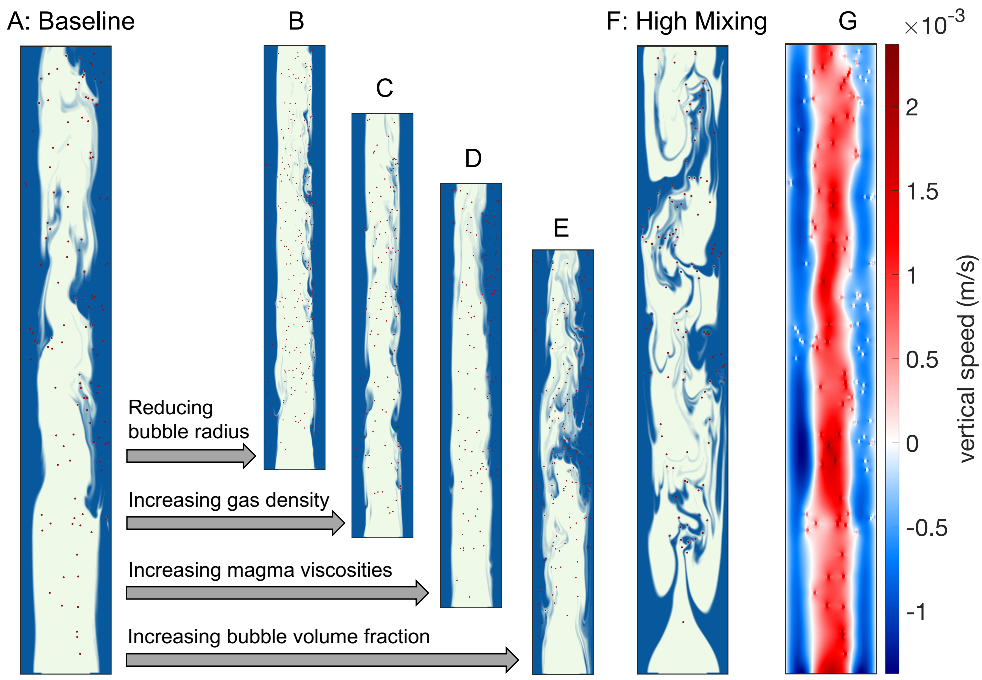

Figure 4. **(A)-(E)**: Snapshots taken at nondimensional time t=40 from simulations No. 1 (A), No. 2 (B), No. 3 (C), No. 5 (D), and No. 14 (E). **(F)**: Snapshot taken at t=6.5 from simulation No. 6, which has highest bubble speed and lowest magma viscosities among simulations in (A)-(F). **(G)**: Corresponding vertical speed field of (A).

We conduct a statistical analysis (fig. 5B) of the simulation results in fig. 5A. Within a period of time $t \in [0, 15]$, where the core-annular flow is stable, we sample points on the interface. At each point, we compute the interfacial stress deviation and the distance to the nearest bubble. We exclude bubble clusters from this analysis, because the hydrodynamic stress field around a bubble cluster is dominated by the diverging interaction forces between bubbles. Fig. 5B shows that the interfacial stress deviation increases as the distance to the nearest bubble decreases, highlighting the significant stress deviation introduced at the interface by nearby bubbles.

As shown in fig. 4F, the presence of bubbles can trigger the collapse of core-annular flow. More specifically, we find two types of collapse in our simulations. Simulation No. 9 shown in fig. 6A demonstrates the type-1 collapse, where a large batch of down-welling, degassed magma drips into the up-welling, volatile-rich magma, disrupting the initially stable core-annular flow. The consequence is a significant amount of mixing, but the flow field itself recovers eventually (fig. 6A). Simulation No. 10 shown in fig. 6B demonstrates the type-2 collapse, where pronounced interfacial waves build up at the beginning of the simulation and quickly lead to seemingly chaotic mixing. In this case, the disrupted core-annular flow never recovers.

3.2 Generalizing Simulation Results through Nondimensional Analysis

To generalize our insights into the physical processes controlling mixing and flow-regime stability in bubble-bearing core-annular flow to various depths within volcanic systems (fig.7B), we identify two nondimensional numbers - the speed ratio $\mathcal{S}$ and the interface stability number $\mathcal{I}$. The speed ratio $\mathcal{S}$ describes the effect of bubble speed by

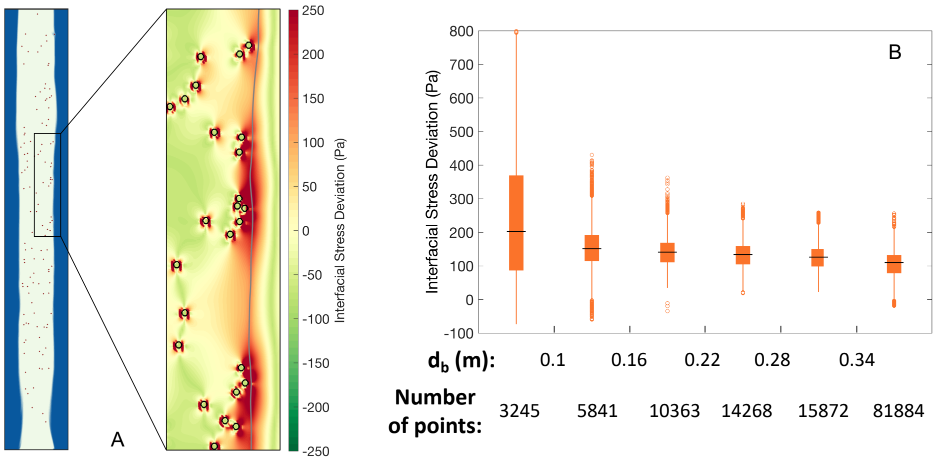

Figure 5. **(A)**: Interfacial stress deviation caused by bubbles (black circles) in the marked subregion of simulation No. 4 at t=6.2. The grey curve marks the interface (c=0.5). **(B)**: Statistical analysis of the relationship between the interfacial shear stress and the vicinity of bubbles for simulation No. 4. Each sample is a point on the interface at $t \in [0, 15]$. d_b is the distance between the sample point and its nearest bubble. The black line segments mark the median (q_2) of each group. The bottom and top of the boxes mark the 25% (q_1) and 75% (q_3) quantiles, respectively. The whiskers mark the range $[q_1 - 1.5 \times (q_3 - q_1), q_3 + 1.5 \times (q_3 - q_1)]$. The circles mark the outliers.

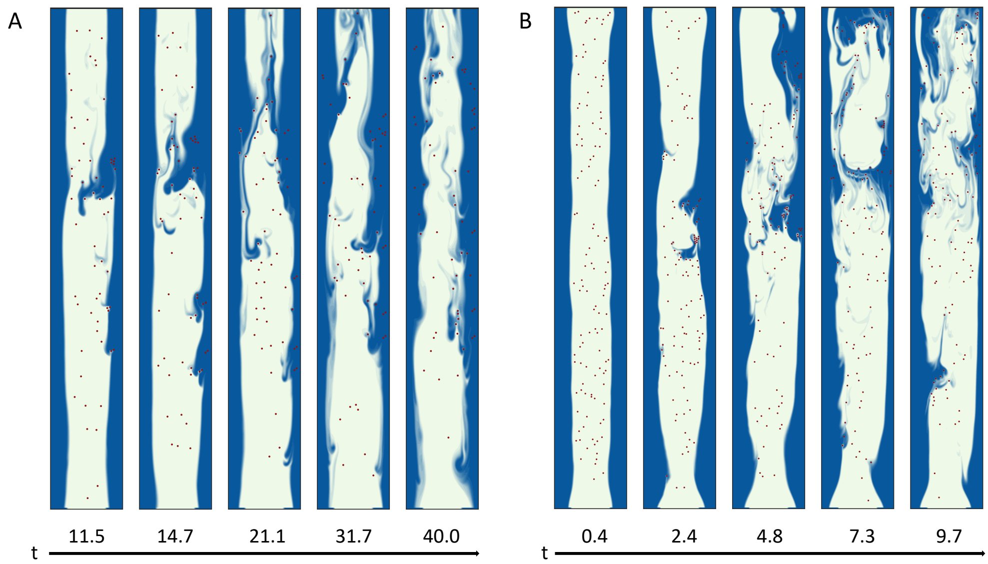

Figure 6. Snapshots from simulations No. 9 (A) and No. 10 (B) showing the collapse of core-annular flow.

comparing v_b with v_c. The interface stability number $\mathcal{I}$ captures the competition of the interfacial shear stress and the magma viscosities. Both nondimensional numbers also incorporate the number of bubbles in the domain. We emphasize that these two numbers are in addition to the more commonly used non-dimensional numbers that characterize the force balance in the flow (e.g., Reynolds number), the bidirectional flow (e.g., Transport number), the domain geometry (e.g., the aspect ratio of the conduit), and the material contrasts between the phases in the flow (e.g., the viscosity contrast).

To estimate the speed ratio and interface stability number, we dimensionalize the non-dimensional, analytical solution of core-annular flow by Suckale et al. (2018). The characteristic speed is

$$U = (\rho_a - \rho_c)gR^2/\mu_a, \tag{12}$$

The interfacial shear stress is

$$\tau = \mu_c \left(\frac{\partial v}{\partial y}\right)_{ndc} \frac{U}{R} = \mu_a \left(\frac{\partial v}{\partial y}\right)_{nda} \frac{U}{R}, \tag{13}$$

where $\left(\frac{\partial v}{\partial y}\right)_{ndc}$ and $\left(\frac{\partial v}{\partial y}\right)_{ndc}$ is the nondimensional lateral component of the vertical speed gradient at the volatile-rich and volatile-poor side of the interface, respectively.

We compute $\mathcal{S}$ by

$$\mathcal{S} = \frac{v_b}{v_c}\frac{\phi R}{r}. \tag{14}$$

Here $\frac{\phi R}{r}$ characterizes the frequency of bubble-interface interaction, which is controlled by the density of bubbles in the domain and thus determined by the domain size (R), bubble volume fraction (ϕ) and bubble size (r).

We compute $\mathcal{I}$ by

$$\mathcal{I} = \frac{\tau^2}{\tau_v^2}\frac{\phi R}{r} = \frac{\tau^2 r}{\mu_c^2 g}\frac{\phi R}{r} = \frac{\left[\left(\frac{\partial v}{\partial y}\right)_{ndc}(\rho_a - \rho_c)\right]^2 \phi g R^3}{\mu_a^2}, \tag{15}$$

which represents the ratio of the interfacial shear stress and the viscous stress multiplied with the frequency of bubble-interface interaction.

We summarize the effect of both non-dimensional numbers on mixing and the stability of the core-annular flow in Fig. 7A. Increasing $\mathcal{S}$ and $\mathcal{I}$ destabilizes the core-annular flow and increases the degree of magma mixing. The decrease of magma mixing and the change from the wavy to stable core-annular flow from simulation No. 1 (fig. 4A) to No. 2 and 3 (figs. 4B-C) are associated with the decrease of $\mathcal{S}$ and $\mathcal{I}$. The decrease of magma mixing from simulation No. 1 (fig. 4A) to No. 5 (fig. 4D) is consistent with the decrease of $\mathcal{I}$. The increase of magma mixing from simulation No. 1 (fig. 4A) to No. 14 (fig. 4E) is consistent with the increase of $\mathcal{S}$ and $\mathcal{I}$. Among simulations shown in fig. 4, simulation No. 6 (fig. 4F) has the largest $\mathcal{S}$ and $\mathcal{I}$ and shows the highest degree of mixing and the most unstable flow regime. The transition zone in fig. 7A shows that the type-1 unstable flow is a transitional scenario between the stable core-annular flow and the type-2 unstable flow that collapses quickly and irreversibly.

The magma properties listed in table 2 demonstrate that shallower depth corresponds to larger $\mathcal{S}$ and $\mathcal{I}$ (fig. 7). As magma ascends, the conduit flow transitions from stable core-annular flow with relatively low mixing to unstable flow with high mixing. The parameters for shallow magma are similar to simulations showing high mixing and unstable flow regime (simulation No. 6 and 10). On the other hand, with limited volatile exsolution, all bubbles in deep magma are likely subgrid-scale. Therefore, we run simulation No. 20 where we we only simulate the two liquid phases to represent the flow in the bottom left region of fig. 7A. The model produces a completely stable core-annular flow regime with low mixing only generated by diffusion, suggesting that bottom left region of fig. 7A corresponds to low mixing and stable core-annular flow regime.

3.3 Magma Mixing Alters H_2O-CO_2 Concentration Profiles

We test the effect of different mixing factors, Γ, and varying CO_2 influx on the H_2O and CO_2 concentrations in melt inclusions by computing the concentration profiles for

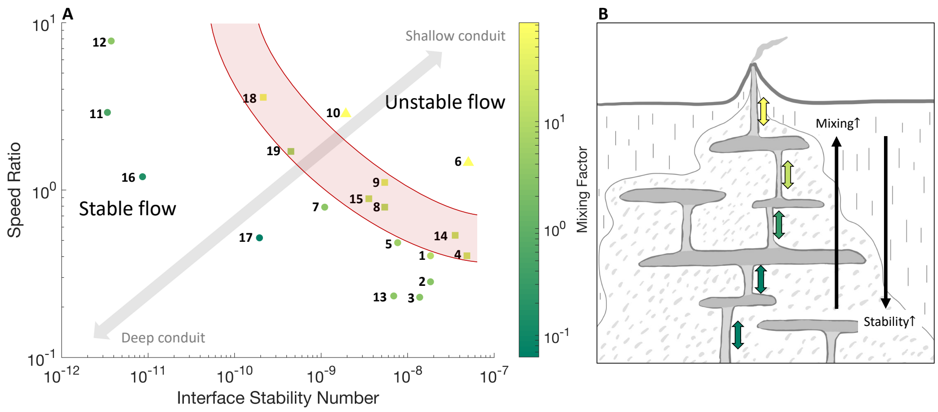

Figure 7. **(A)**: Regime diagram for the stability of core-annular flow. The numbers identify individual simulations and the color scale represents the mixing factor Γ. Round, square and triangle markers highlight stable, type-1 unstable, and type-2 unstable core-annular flow during $t \in [0, 90]$, respectively, The inferred red transition zone covering the type-1 unstable flow separates the stable and unstable flow. **(B)**: Our model indicates higher degree of mixing and less stable flow regime in the conduits towards shallower depth.

Stromboli and Mount Erebus. To compare the two processes, we conduct two suites of calculations for each volcano. In each group, we fix one process and vary the other one to test whether the two processes have distinct observational signatures. In both cases, we fix the total amount of H_2O as the concentrations in the most volatile-rich melt inclusions, because at P_{max} H_2O is unsaturated according to MagmaSat (Gualda et al., 2012; Ghiorso & Gualda, 2015).

Fig. 8 compares the computed volatile concentration profiles to existing data (Métrich et al., 2010; Oppenheimer et al., 2011). Even small degrees of mixing ($\Gamma < 5\%$) sensitively affect the functional relationship between the CO_2 and the H_2O (figs. 8A-B). Increasing mixing shifts the concentration profiles towards higher CO_2 and lower H_2O concentration relative to the closed-system profiles ($\Gamma = 0$). However, the profiles quickly become insensitive to further mixing as shown by the profiles with Γ=20% in figs. 8A-B. With $\Gamma > 30\%$, stable core-annular flow no longer exists in our simulations (fig. 7A). Therefore, we only compute profiles with mixing factors below this limit. While we have evaluated both constant and depth-variable mixing factors, both results are consistent with data, suggesting that the data does not currently afford the resolution necessary to identify potential depth-variability in mixing (figs. 8A-B).

Accounting for magma mixing results in concentration profiles that are more consistent with the Stromboli data and sample 97009 from Mount Erebus than open- or closed-system degassing alone (figs. 8A-B). Samples other than 97009 from Mount Erebus match a closed-system profile (black dots in fig. 8A) and clearly distinct sample 97009. However, we are unable to constrain the mixing factor through the melt inclusion data exactly due to data scatter. When analyzing the effect of variable CO_2 influx, we therefore only consider minimal mixing, Γ=1%. Figs. 8C and D show that for a fixed Γ=1%, varying CO_2 influx also significantly alters the volatile concentration profiles and further improves the fit between model and data. Increasing CO_2 influx shifts the profiles towards higher CO_2 and lower H_2O concentration, especially at high pressures. This effect is distinct from the effect of magma mixing.

Varying CO_2 influx also changes the ratio of H_2O and CO_2 in the gas phase in our calculations. In the legend of figs. 8C and D, we include the values of λ=H_2O/CO_2 in the gas phase at the surface in each calculation. According to the surface gas flux data, λ ranges from 0.82 to 2.49 and 0.56 to 0.79 at Stromboli and Mount Erebus, respectively (Burton, Allard, et al., 2007; Oppenheimer et al., 2009).

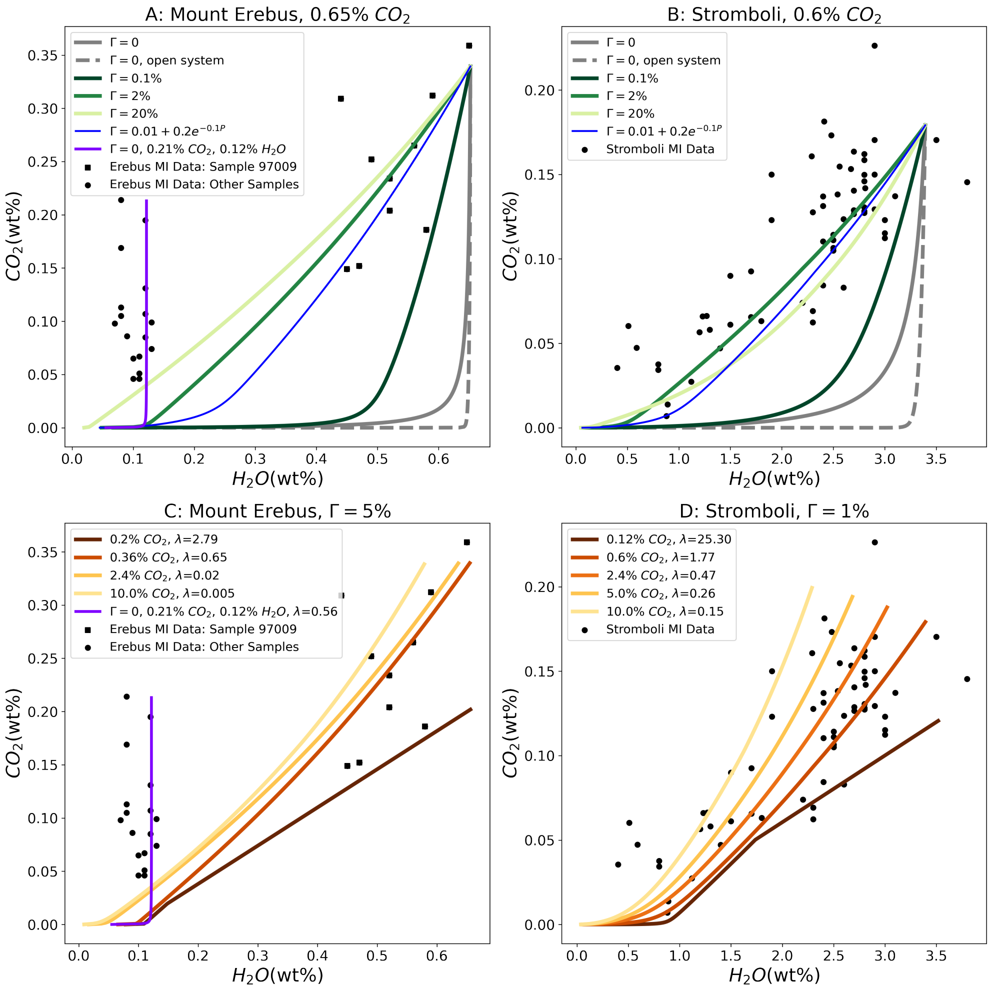

Figure 8. H_2O-CO_2 concentration profiles with varied mixing factors (A and B) and total amount of CO_2 (C and D). The blue curves in A and B represents profiles with mixing factors varied with pressure.

4 Discussion

Analogue laboratory models illustrate the basic physical processes that govern bidirectional flow (Stevenson & Blake, 1998; Beckett et al., 2011), but are highly idealized representations of actual volcanic systems. Conduit models can help bridge the gap (Suckale et al., 2018; Fowler & Robinson, 2018), but are difficult to test against observational data. The challenge arises because observational data, such as melt inclusion compositions and surface gas flux (Métrich et al., 2001; Burton, Allard, et al., 2007; Oppenheimer et al., 2009; Métrich et al., 2010; Oppenheimer et al., 2011; Ilanko et al., 2015; Rasmussen et al., 2017), are the product of multi-scale processes while most existing conduit models are single-scale and do not entail testable model predictions at the scale of individual bubbles or crystals.

In this study, we integrate numerical simulations of bidirectional conduit flow at the scale of individual bubbles with a system-scale calculation of H_2O-CO_2 concentration profiles. We analyze how the presence of bubbles affects the degree of magma mixing in a conduit segment (fig. 4). Previous experimental and numerical studies show that the viscosity contrast (μ_c/μ_a) governs the stability of the flow regime (Stevenson & Blake, 1998; Suckale et al., 2018). Here, we demonstrate that the properties of the gas phase are important, too. Bubbles with a sufficient rise speed can trigger significant mixing and even flow-regime collapse at viscosity contrasts that are stable in the absence of bubbles (Stevenson & Blake, 1998; Suckale et al., 2018).

While there is not doubt that viscosity contrast is important for the stability of core-annular flow as suggested by previous studies (Stevenson & Blake, 1998; Suckale et al., 2018), our results indicate that two nondimensional numbers, $\mathcal{S}$ and $\mathcal{I}$, are valuable additions to consider. Simulations with the same viscosity contrast ($\frac{\mu_a}{\mu_c} = 3$ for simulations No. 1-6, 13, 14, $\frac{\mu_a}{\mu_c} = 10$ for simulations No. 7-10, 15, 17, $\frac{\mu_a}{\mu_c} = 20$ for simulations No. 18-19) show significantly varied mixing and stability. This variance is well captured by $\mathcal{S}$ and $\mathcal{I}$ (fig. 7).

We argue that bubbles locally increase the interfacial stress (fig. 5). This interfacial stress deviation disrupts the linearly unstable (Selvam et al., 2007; Martin et al., 2009; Selvam et al., 2009) but nonlinearly stable interface (Ullmann & Brauner, 2004; Suckale et al., 2018). In the absence of bubbles, linear growth of instability is suppressed by the nonlinear interaction between the growing interface wave and viscous damping in the two magmas (Ullmann & Brauner, 2004; Suckale et al., 2018). We show that the presence of bubbles introduces additional perturbations into this metastable flow configuration (e.g., fig. 4B) that can trigger wave breaking (e.g., fig. 4A) and mixing (e.g., fig. 4F).

The finding that bubbles with radii much smaller than the conduit width can have such a significant effect may appear surprising. However, flow-regime stability at the conduit scale ultimately hinges on interface stability, which in turn hinges on the disruptions introduced by the bubbles. The relevant scale comparison is thus not between bubble radius and conduit width, but between bubble radius and the amplitude of the interfacial wave. So long as a well-defined interface exists, these scales are comparable (Ullmann & Brauner, 2004; Suckale et al., 2018). We emphasize that we only simulate magmas with low diffusivities here, similar to Stevenson and Blake (1998).

Our simulations suggest that some degree of mixing is almost inevitable in core-annular flow unless bubbles remain very small, which could occur particularly for very low H_2O contents. Magma mixing tend to increase at shallow depth, potentially to the point of core-annular flow collapse (fig. 7). The reason is that the gas phase plays an increasingly important role in the system dynamics at decreasing depth below the surface, because of continued exsolution, bubble growth, and gas decompression (e.g., Gonnermann & Manga, 2013).

If magma mixing is as common as our simulations suggest, it would be reflected in observational data. To test the compatibility of our model results with observations, we compute the H_2O-CO_2 concentration profiles associated with different mixing factors building on Witham (2011a). The fit between modeled and measured volatile concentrations increases notably when accounting for magma mixing, even for low mixing factors (figs. 8A-B).

Figs. 8C-D show that varying CO_2 influx also improves the match between modeled and measured volatile concentrations, as also argued by previous studies (e.g., Burton, Mader, & Polacci, 2007; Métrich et al., 2010; Rasmussen et al., 2017). Both Burton, Mader, and Polacci (2007) and Métrich et al. (2010) estimate that the amount of CO_2

influx at Stromboli is 2.4%. In our simulations, this CO_2 influx results in a λ=0.47 (H_2O/CO_2 in the gas phase at the surface) as shown in fig. 8D. Even with a low degree of mixing, this resultant λ is outside the range 0.82-2.49 observed at Stromboli (Burton, Allard, et al., 2007). Increased mixing further decreases λ due to more loss of H_2O to the downwelling magma. We argue here that when accounting for magma mixing, it is unnecessary to invoke a large amount of CO_2 for reproducing melt inclusion data (Métrich et al., 2010; Rasmussen et al., 2017). Fig. 8D shows that a CO_2 influx of 0.6% results in a λ=1.77, which is in the observed range (Burton, Allard, et al., 2007).

For Erebus, most samples are H_2O-poor except sample 97009 (Oppenheimer et al., 2011). Oppenheimer et al. (2011) propose that Mount Erebus is occasionally fed by volatile-rich magma but continuously flushed by CO_2-rich fluid. The resultant dry magma leads to high magma viscosity and thus low mixing. This idea is compatible with our model results: The purple curve in figs. 8A and C shows that the closed-system profile matches the data. Assuming complete degassing of CO_2 and H_2O, the calculated λ matches the surface gas flux measurements. Sample 97009 may have formed shortly after the injection of volatile-rich magma, which decreases magma viscosity and increases mixing.

We emphasize that apart from magma mixing and variable CO_2 influx, several other processes not considered in our study contribute to the pronounced scatter in melt inclusion data. These include uncertainties in measurements (Métrich & Wallace, 2008; Métrich et al., 2010; Oppenheimer et al., 2011), disequilibrium degassing potentially generating CO_2-oversaturated melt (Pichavant et al., 2013) and crystallization affecting volatile solubility (Gualda et al., 2012; Ghiorso & Gualda, 2015). In addition, the complex geometry of some volcanic plumbing systems may introduce variability. At shallow depth, some conduits flare out into lava lakes such as at Mount Erebus, altering both mixing and surface gas flux (Oppenheimer et al., 2009). At deep depth, volcanic conduits are thought to be connected to heterogeneous and largely crystalline transcrustal plumbing systems (Cashman et al., 2017; Magee et al., 2018). Melt inclusions that form at considerable depth (Métrich et al., 2001, 2010; Oppenheimer et al., 2011; Rasmussen et al., 2017) might hence sample a different portion of the plumbing system and record processes not considered here.

Despite these caveats, our analysis suggests that melt inclusions might offer the opportunity to constrain magma mixing in volcanic conduits and variations in CO_2 influx over time. Both of these processes contribute to variability in the surface gas flux, which is correlated with the eruptive cycles of persistently degassing volcanoes (Burton, Allard, et al., 2007; Oppenheimer et al., 2009; Ilanko et al., 2015). Constraining their inherent variability over multiple eruptive cycles hence has the potential for increasing the constraints we can bring to bear in conduit-flow models. We hence suggest that with improved measurement accuracy and reduced uncertainty, disaggregating the scattered melt inclusion data could help us track and better understand the evolving flow conditions in volcanic conduits, as already attempted in Spilliaert et al. (2006) and Sides et al. (2014).

5 Conclusions

Observables such as melt inclusions provide important testimony on degassing processes at persistently active volcanoes, but their testimony is rarely straight-forward to interpret. Models such as bidirectional conduit flow, on the other hand, account for important physical processes, but are difficult to connect to and evaluate against observational data. This study contributes towards forging a closer link between a commonly used and theoretically well-motivated conduit model for persistent degassing, core-annular flow, and the volatile concentration observed in melt-inclusion data. We find that bubbles that are large enough to decouple from the ambient flow field and ascend individually can destabilize the bidirectional flow and can lead to significant mixing between volatile-rich and volatile-poor magma. This finding suggests that magma mixing is common in core-annular flow in the conduits of persistently degassing volcanoes, but variations in CO_2 influx may occur simultaneously. Being able to identify the relative importance of these two processes in observational data is valuable to track and better understand the evolving flow conditions in volcanic systems. Our study shows that while both magma mixing and increasing CO_2 influx shifts the profiles towards higher CO_2 and lower H_2O concentration, the observational signature of increasing CO_2 influx is distinct from that of magma mixing by being most prominent at high pressures. Disaggregating scattered melt inclusion data for different volcanic centers or eruptive episodes may hence help to identify variability in degassing.

Acknowledgments

This work is supported by NSF grant 1744758 awarded to JS and by the Stanford Graduate Fellowship in Science and Engineering awarded to ZW. We thank Sandro Aiuppa and other anonymous reviewers for providing thoughtful suggestions for improving this manuscript. We thank Ayla Pamukcu for providing feedback to improve the text, and Mark Ghiorso for providing access to ENKI server.

Open Research

v1.0.7 of the code used for the conduit-flow model and the volatile-concentration model is preserved at `https://doi.org/10.5281/zenodo.5090109` with open access. The usage instructions are provided in the README file of the repository.

Author contributions

Z.W. performed the numerical simulations, computed the concentration profiles, produced the figures and wrote most of the text. Z.Q. developed the numerical technique. J.S. conceptualized the study, advised Z.W. and contributed to the text.

References

Allard, P., Carbonnelle, J., Métrich, N., Loyer, H., & Zettwoog, P. (1994, 03). Sulfur output and magma degassing budget of stromboli volcano. *Nature*, *368*, 326-330. doi: 10.1038/368326a0

Aster, E. M., Wallace, P. J., Moore, L. R., Watkins, J., Gazel, E., & Bodnar, R. J. (2016). Reconstructing co2 concentrations in basaltic melt inclusions using raman analysis of vapor bubbles. *Journal of Volcanology and Geothermal Research*, *323*, 148 - 162. Retrieved from `http://www.sciencedirect.com/science/article/pii/S0377027316300701` doi: https://doi.org/10.1016/j.jvolgeores.2016.04.028

Barth, A., Newcombe, M., Plank, T., Gonnermann, H., Hajimirza, S., Soto, G. J., ... Hauri, E. (2019). Magma decompression rate correlates with explosivity at basaltic volcanoes — constraints from water diffusion in olivine. *Journal of Volcanology and Geothermal Research*, *387*, 106664. Retrieved from `http://www.sciencedirect.com/science/article/pii/S0377027319301192` doi: https://doi.org/10.1016/j.jvolgeores.2019.106664

Beckett, F. M., Mader, H. M., Phillips, J. C., Rust, A. C., & Witham, F. (2011). An experimental study of low-reynolds-number exchange flow of two newtonian fluids in a vertical pipe. *Journal of Fluid Mechanics*, *682*, 652–670. doi: 10.1017/jfm.2011.264

Bertagnini, A., Métrich, N., Landi, P., & Rosi, M. (2003). Stromboli volcano (aeolian archipelago, italy): An open window on the deep-feeding system of a steady state basaltic volcano. *Journal of Geophysical Research: Solid Earth*, *108*(B7). Retrieved from `https://agupubs.onlinelibrary.wiley.com/doi/abs/10.1029/2002JB002146` doi: 10.1029/2002JB002146

Blake, S., & Campbell, I. H. (1986, Sep 01). The dynamics of magma-mixing during flow in volcanic conduits. *Contributions to Mineralogy and Petrology*, *94*(1), 72-81. Retrieved from https://doi.org/10.1007/BF00371228 doi: 10.1007/BF00371228

Blundy, J., Cashman, K. V., Rust, A., & Witham, F. (2010). A case for co2-rich arc magmas. *Earth and Planetary Science Letters*, *290*(3), 289 - 301. Retrieved from http://www.sciencedirect.com/science/article/pii/S0012821X09007365 doi: https://doi.org/10.1016/j.epsl.2009.12.013

Bowen, R. M. (1976). Theory of mixtures. In *Part i: Continuum physics* (pp. 1–127). Academic Press, New York, USA.

Bucholz, C. E., Gaetani, G. A., Behn, M. D., & Shimizu, N. (2013). Post-entrapment modification of volatiles and oxygen fugacity in olivine-hosted melt inclusions. *Earth and Planetary Science Letters*, *374*, 145 - 155. Retrieved from http://www.sciencedirect.com/science/article/pii/S0012821X13002781 doi: https://doi.org/10.1016/j.epsl.2013.05.033

Burton, M., Allard, P., Muré, F., & La Spina, A. (2007). Magmatic gas composition reveals the source depth of slug-driven strombolian explosive activity. *Science*, *317*(5835), 227–230. Retrieved from http://science.sciencemag.org/content/317/5835/227 doi: 10.1126/science.1141900

Burton, M., Mader, H., & Polacci, M. (2007). The role of gas percolation in quiescent degassing of persistently active basaltic volcanoes. *Earth and Planetary Science Letters*, *264*(1), 46 - 60. Retrieved from http://www.sciencedirect.com/science/article/pii/S0012821X07005493 doi: https://doi.org/10.1016/j.epsl.2007.08.028

Cashman, K. V., Sparks, R. S. J., & Blundy, J. D. (2017). Vertically extensive and unstable magmatic systems: A unified view of igneous processes. *Science*, *355*(6331). Retrieved from https://science.sciencemag.org/content/355/6331/eaag3055 doi: 10.1126/science.aag3055

Del Bello, E., Llewellin, E. W., Taddeucci, J., Scarlato, P., & Lane, S. J. (2012). An analytical model for gas overpressure in slug-driven explosions: Insights into strombolian volcanic eruptions. *Journal of Geophysical Research: Solid Earth*, *117*(B2). Retrieved from https://agupubs.onlinelibrary.wiley.com/doi/abs/10.1029/2011JB008747 doi: https://doi.org/10.1029/2011JB008747

Dibble, R. R., BARRETT, S. I., Kaminuma, K., Miura, S., Kienle, J., Rowe, C. A., ... Mcintosh, W. C. (1988). Time comparisons between video and seismic signals from explosions in the lava lake of erebus volcano, antarctica. *Bulletin of the Disaster Prevention Research Institute*, *38*(3), 147–161.

DiBenedetto, M., Qin, Z., & Suckale, J. (2020). Crystal aggregates record the pre-eruptive flow field in the volcanic conduit at kilauea, hawaii. *Science Advances*, *6*(49). Retrieved from https://advances.sciencemag.org/content/6/49/eabd4850 doi: 10.1126/sciadv.abd4850

Dixon, J., M. Stolper, E., & Clague, D. (1991, 05). Degassing history of water, sulfur, and carbon in submarine lavas from kilauea volcano, hawaii. *Journal of Geology*, *99*. doi: 10.1086/629501

Fowler, A., & Robinson, M. (2018). Counter-current convection in a volcanic conduit. *Journal of Volcanology and Geothermal Research*, *356*, 141 - 162. Retrieved from http://www.sciencedirect.com/science/article/pii/S0377027317304274 doi: https://doi.org/10.1016/j.jvolgeores.2018.03.004

Francis, P., Oppenheimer, C., & Stevenson, D. (1993, 12). Endogenous growth of persistently active volcanoes. *Nature*, *366*, 554-557. doi: 10.1038/366554a0

Ghiorso, M. S., & Gualda, G. A. R. (2015). An h2o–co2 mixed fluid saturation model compatible with rhyolite-melts. *Contributions to Mineralogy and Petrology*, *169*(6), 53. Retrieved from https://doi.org/10.1007/s00410-015-1141-8 doi: 10.1007/s00410-015-1141-8

Giordano, D., Russell, J. K., & Dingwell, D. B. (2008). Viscosity of magmatic liquids: A model. *Earth and Planetary Science Letters*, *271*(1), 123 - 134. Retrieved from http://www.sciencedirect.com/science/article/pii/

S0012821X08002240 doi: https://doi.org/10.1016/j.epsl.2008.03.038
Gonnermann, H., & Manga, M. (2013). Dynamics of magma ascent in the volcanic conduit. In *Modeling volcanic processes: The physics and mathematics of volcanism* (pp. 55–84).
Gualda, G. A. R., Ghiorso, M. S., Lemons, R. V., & Carley, T. L. (2012). Rhyolite-melts: a modified calibration of melts optimized for silica-rich, fluid-bearing magmatic systems. *Journal of Petrology*, *53*(5), 875-890. Retrieved from http://dx.doi.org/10.1093/petrology/egr080 doi: 10.1093/petrology/egr080
Ilanko, T., Oppenheimer, C., Burgisser, A., & Kyle, P. (2015). Transient degassing events at the lava lake of erebus volcano, antarctica: Chemistry and mechanisms. *GeoResJ*, *7*, 43 - 58. Retrieved from http://www.sciencedirect.com/science/article/pii/S2214242815000327 doi: https://doi.org/10.1016/j.grj.2015.05.001
Jaupart, C., & Vergniolle, S. (1988, Jan 01). Laboratory models of hawaiian and strombolian eruptions. *Nature*, *331*(6151), 58-60. Retrieved from https://doi.org/10.1038/331058a0 doi: 10.1038/331058a0
Johnson, J., Aster, R., Jones, K. R., Kyle, P., & McIntosh, B. (2008). Acoustic source characterization of impulsive strombolian eruptions from the mount erebus lava lake. *Journal of Volcanology and Geothermal Research*, *177*(3), 673 - 686. Retrieved from http://www.sciencedirect.com/science/article/pii/S0377027308003727 (Volcanology of Erebus volcano, Antarctica) doi: https://doi.org/10.1016/j.jvolgeores.2008.06.028
Kazahaya, K., Shinohara, H., & Saito, G. (1994, Aug 01). Excessive degassing of izu-oshima volcano: magma convection in a conduit. *Bulletin of Volcanology*, *56*(3), 207–216. Retrieved from https://doi.org/10.1007/BF00279605 doi: 10.1007/BF00279605
Kyle, P. R. (1977). Mineralogy and glass chemistry of recent volcanic ejecta from mt erebus, ross island, antarctica. *New Zealand Journal of Geology and Geophysics*, *20*(6), 1123-1146. Retrieved from https://doi.org/10.1080/00288306.1977.10420699 doi: 10.1080/00288306.1977.10420699
Levine, A., Ramaswamy, S., Frey, E., & Bruinsma, R. (1998). Screened and unscreened phases in sedimenting suspensions. *Physical review letters*, *81*(26), 5944.
Liu, Y., Anderson, A., Wilson, C., Davis, A., & Steele, I. (2006, 12). Mixing and differentiation in the oruanui rhyolitic magma, taupo, new zealand: Evidence from volatiles and trace elements in melt inclusions. *Contributions to Mineralogy and Petrology*, *151*, 71-87. doi: 10.1007/s00410-005-0046-3
Magee, C., Stevenson, C. T. E., Ebmeier, S. K., Keir, D., Hammond, J. O. S., Gottsmann, J. H., ... Jackson, M. D. (2018, 06). Magma Plumbing Systems: A Geophysical Perspective. *Journal of Petrology*, *59*(6), 1217-1251. Retrieved from https://doi.org/10.1093/petrology/egy064 doi: 10.1093/petrology/egy064
Martin, J., Rakotomalala, N., Salin, D., & Talon, L. (2009). Convective/absolute instability in miscible core-annular flow. part 1: Experiments. *Journal of fluid mechanics*, *618*, 305.
McBirney, A. R., & Murase, T. (1984). Rheological properties of magmas. *Annual Review of Earth and Planetary Sciences*, *12*(1), 337–357.
Métrich, N., Bertagnini, A., Landi, P., & Rosi, M. (2001). Crystallization driven by decompression and water loss at stromboli volcano (aeolian islands, italy). *Journal of Petrology*, *42*(8), 1471-1490. Retrieved from http://dx.doi.org/10.1093/petrology/42.8.1471 doi: 10.1093/petrology/42.8.1471
Métrich, N., Bertagnini, A., & Muro, A. (2010). Conditions of magma storage, degassing and ascent at stromboli: New insights into the volcano plumbing system with inferences on the eruptive dynamics. *Journal of Petrology*, *51*,

603-626. doi: 10.1093/petrology/egp083
Métrich, N., & Wallace, P. J. (2008). Volatile abundances in basaltic magmas and their degassing paths tracked by melt inclusions. *Reviews in Mineralogy and Geochemistry*, *69*, 363 - 402. doi: https://doi.org/10.2138/rmg.2008.69.10
Molina, I., Burgisser, A., & Oppenheimer, C. (2012). Numerical simulations of convection in crystal-bearing magmas: A case study of the magmatic system at erebus, antarctica. *Journal of Geophysical Research: Solid Earth*, *117*(B7). Retrieved from https://agupubs.onlinelibrary.wiley.com/doi/abs/10.1029/2011JB008760 doi: 10.1029/2011JB008760
Moussallam, Y., Bani, P., Curtis, A., Barnie, T., Moussallam, M., Peters, N., ... Cardona, C. (2016). Sustaining persistent lava lakes: Observations from high-resolution gas measurements at villarrica volcano, chile. *Earth and Planetary Science Letters*, *454*, 237 - 247. Retrieved from http://www.sciencedirect.com/science/article/pii/S0012821X16304927 doi: https://doi.org/10.1016/j.epsl.2016.09.012
Métrich, N., Allard, P., Bertagnini, A., & Muro], A. D. (2011). Comment on 'conduit convection, magma mixing, and melt inclusion trends at persistent degassing volcanoes' by fred witham, published in earth planetary science letters (2011) 301, 345–352. *Earth and Planetary Science Letters*, *306*(3), 306 - 308. Retrieved from http://www.sciencedirect.com/science/article/pii/S0012821X11002287 doi: https://doi.org/10.1016/j.epsl.2011.04.012
Oppenheimer, C., Lomakina, A. S., Kyle, P. R., Kingsbury, N. G., & Boichu, M. (2009). Pulsatory magma supply to a phonolite lava lake. *Earth and Planetary Science Letters*, *284*(3), 392 - 398. Retrieved from http://www.sciencedirect.com/science/article/pii/S0012821X09002805 doi: https://doi.org/10.1016/j.epsl.2009.04.043
Oppenheimer, C., Moretti, R., Kyle, P. R., Eschenbacher, A., Lowenstern, J. B., Hervig, R. L., & Dunbar, N. W. (2011). Mantle to surface degassing of alkalic magmas at erebus volcano, antarctica. *Earth and Planetary Science Letters*, *306*(3), 261 - 271. Retrieved from http://www.sciencedirect.com/science/article/pii/S0012821X11002111 doi: https://doi.org/10.1016/j.epsl.2011.04.005
Palma, J. L., Calder, E. S., Basualto, D., Blake, S., & Rothery, D. A. (2008). Correlations between SO2 flux, seismicity, and outgassing activity at the open vent of Villarrica volcano, Chile. *Journal of Geophysical Research*, *113*, B10201.
Pichavant, M., Di Carlo, I., Rotolo, S. G., Scaillet, B., Burgisser, A., Le Gall, N., & Martel, C. (2013, Aug 01). Generation of co2-rich melts during basalt magma ascent and degassing. *Contributions to Mineralogy and Petrology*, *166*(2), 545-561. Retrieved from https://doi.org/10.1007/s00410-013-0890-5 doi: 10.1007/s00410-013-0890-5
Qin, Z., Allison, K., & Suckale, J. (2020). Direct numerical simulations of viscous suspensions with variably shaped crystals. *Journal of Computational Physics*, *401*, 109021. Retrieved from https://www.sciencedirect.com/science/article/pii/S0021999119307272 doi: https://doi.org/10.1016/j.jcp.2019.109021
Qin, Z., Soldati, A., Velazquez Santana, L. C., Rust, A. C., Suckale, J., & Cashman, K. V. (2018). Slug stability in flaring geometries and ramifications for lava lake degassing. *Journal of Geophysical Research: Solid Earth*, *123*(12), 10,431-10,448. Retrieved from https://agupubs.onlinelibrary.wiley.com/doi/abs/10.1029/2018JB016113 doi: 10.1029/2018JB016113
Qin, Z., & Suckale, J. (2017). Direct numerical simulations of gas–solid–liquid interactions in dilute fluids. *International Journal of Multiphase Flow*, *96*, 34 - 47. doi: https://doi.org/10.1016/j.ijmultiphaseflow.2017.07.008
Qin, Z., & Suckale, J. (2020). Flow-to-sliding transition in crystal-bearing magma. *Journal of Geophysical Research: Solid Earth*, *125*(2), e2019JB018549.

Rasmussen, D. J., Kyle, P. R., Wallace, P. J., Sims, K. W. W., Gaetani, G. A., & Phillips, E. H. (2017, 08). Understanding Degassing and Transport of CO2-rich Alkalic Magmas at Ross Island, Antarctica using Olivine-Hosted Melt Inclusions. *Journal of Petrology*, *58*(5), 841-861. Retrieved from `https://dx.doi.org/10.1093/petrology/egx036` doi: 10.1093/petrology/egx036

Ripepe, M., Donne, D. D., Genco, R., Maggio, G., Pistolesi, M., Marchetti, E., ... Poggi, P. (2015, May 18). Volcano seismicity and ground deformation unveil the gravity-driven magma discharge dynamics of a volcanic eruption. *Nature Communications*, *6*(1), 6998. Retrieved from `https://doi.org/10.1038/ncomms7998` doi: 10.1038/ncomms7998

Ruth, D. C. S., Costa, F., Bouvet de Maisonneuve, C., Franco, L., Cortés, J. A., & Calder, E. S. (2018, Jul 09). Crystal and melt inclusion timescales reveal the evolution of magma migration before eruption. *Nature Communications*, *9*(1), 2657. doi: 10.1038/s41467-018-05086-8

Schmitt, A. K. (2001). Gas-saturated crystallization and degassing in large-volume, crystal-rich dacitic magmas from the altiplano-puna, northern chile. *Journal of Geophysical Research: Solid Earth*, *106*(B12), 30561-30578. Retrieved from `https://agupubs.onlinelibrary.wiley.com/doi/abs/10.1029/2000JB000089` doi: 10.1029/2000JB000089

Segre, P., Herbolzheimer, E., & Chaikin, P. (1997). Long-range correlations in sedimentation. *Physical Review Letters*, *79*(13), 2574.

Selvam, B., Merk, S., Govindarajan, R., & Meiburg, E. (2007). Stability of miscible core–annular flows with viscosity stratification. *Journal of Fluid Mechanics*, *592*, 23–49.

Selvam, B., Talon, L., Lesshafft, L., & Meiburg, E. (2009). Convective/absolute instability in miscible core-annular flow. part 2. numerical simulations and nonlinear global modes. *Journal of fluid mechanics*, *618*, 323.

Shinohara, H. (2008). Excess degassing from volcanoes and its role on eruptive and intrusive activity. *Reviews of Geophysics*, *46*(4). Retrieved from `https://agupubs.onlinelibrary.wiley.com/doi/abs/10.1029/2007RG000244` doi: https://doi.org/10.1029/2007RG000244

Sides, I., Edmonds, M., Maclennan, J., Houghton, B., Swanson, D., & Steele-MacInnis, M. (2014). Magma mixing and high fountaining during the 1959 kīlauea iki eruption, hawai'i. *Earth and Planetary Science Letters*, *400*, 102 - 112. Retrieved from `http://www.sciencedirect.com/science/article/pii/S0012821X14003264` doi: https://doi.org/10.1016/j.epsl.2014.05.024

Spilliaert, N., Métrich, N., & Allard, P. (2006). S–cl–f degassing pattern of water-rich alkali basalt: modelling and relationship with eruption styles on mount etna volcano. *Earth and Planetary Science Letters*, *248*(3-4), 772–786.

Stevenson, D. S., & Blake, S. (1998, Nov 01). Modelling the dynamics and thermodynamics of volcanic degassing. *Bulletin of Volcanology*, *60*(4), 307–317. Retrieved from `https://doi.org/10.1007/s004450050234` doi: 10.1007/s004450050234

Stoiber, R., & Williams, S. (1986). Sulfur and halogen gases at Masaya caldera complex, Nicaragua: total flux and variations with time. *Journal of Geophysical Research*, *91*, 12,215-12,231.

Suckale, J., Qin, Z., Picchi, D., Keller, T., & Battiato, I. (2018). Bistability of buoyancy-driven exchange flows in vertical tubes. *Journal of Fluid Mechanics*, *850*, 525–550. doi: 10.1017/jfm.2018.382

Sweeney, D., Kyle, P. R., & Oppenheimer, C. (2008). Sulfur dioxide emissions and degassing behavior of erebus volcano, antarctica. *Journal of Volcanology and Geothermal Research*, *177*(3), 725 - 733. Retrieved from `http://www.sciencedirect.com/science/article/pii/S0377027308000553` (Volcanology of Erebus volcano, Antarctica) doi: https://doi.org/10.1016/j.jvolgeores.2008.01.024

Tong, P., & Ackerson, B. J. (1998). Analogies between colloidal sedimentation and turbulent convection at high prandtl numbers. *Physical Review E*, *58*(6), R6931.

Tryggvason, G., Dabiri, S., Aboulhasanzadeh, B., & Lu, J. (2013). Multiscale considerations in direct numerical simulations of multiphase flows. *Physics of Fluids*, *25*(3), 031302. Retrieved from `https://doi.org/10.1063/1.4793543` doi: 10.1063/1.4793543

Ullmann, A., & Brauner, N. (2004). Closure relations for the shear stress in two-fluid models for core-annular flow. *Multiphase Science and Technology*, *16*(4).

Wallace, P. J. (2005). Volatiles in subduction zone magmas: concentrations and fluxes based on melt inclusion and volcanic gas data. *Journal of Volcanology and Geothermal Research*, *140*(1), 217 - 240. Retrieved from `http://www.sciencedirect.com/science/article/pii/S0377027304002884` (Energy and Mass Fluxes in Volcanic Arcs) doi: https://doi.org/10.1016/j.jvolgeores.2004.07.023

Wei, Z., Qin, Z., & Suckale, J. (2021). *Code repo for "Magma mixing during conduit flow is reflected in melt-inclusion data from persistently degassing volcanoes".* Zenodo. Retrieved from `https://doi.org/10.5281/zenodo.5090109` doi: 10.5281/zenodo.5090109

Witham, F. (2011a). Conduit convection, magma mixing, and melt inclusion trends at persistently degassing volcanoes. *Earth and Planetary Science Letters*, *301*(1), 345 - 352. Retrieved from `http://www.sciencedirect.com/science/article/pii/S0012821X10007120` doi: https://doi.org/10.1016/j.epsl.2010.11.017

Witham, F. (2011b). Conduit convection, magma mixing, and melt inclusion trends at persistently degassing volcanoes: Reply to comment by métrich et al. (2011). *Earth and Planetary Science Letters*, *306*(3), 309 - 311. Retrieved from `http://www.sciencedirect.com/science/article/pii/S0012821X11002366` doi: https://doi.org/10.1016/j.epsl.2011.04.020

Woitischek, J., Woods, A. W., Edmonds, M., Oppenheimer, C., Aiuppa, A., Pering, T. D., ... Garaebiti, E. (2020). Strombolian eruptions and dynamics of magma degassing at yasur volcano (vanuatu). *Journal of Volcanology and Geothermal Research*, *398*, 106869.

Xue, J.-Z., Herbolzheimer, E., Rutgers, M., Russel, W., & Chaikin, P. (1992). Diffusion, dispersion, and settling of hard spheres. *Physical review letters*, *69*(11), 1715.

Yoshimura, S. (2015). Diffusive fractionation of h2o and co2 during magma degassing. *Chemical Geology*, *411*, 172 - 181. Retrieved from `http://www.sciencedirect.com/science/article/pii/S0009254115003228` doi: https://doi.org/10.1016/j.chemgeo.2015.07.003

Zhang, Y., & Stolper, E. M. (1991). Water diffusion in a basaltic melt. *Nature*, *351*(6324), 306-309. Retrieved from `https://doi.org/10.1038/351306a0` doi: 10.1038/351306a0

Figure 1.

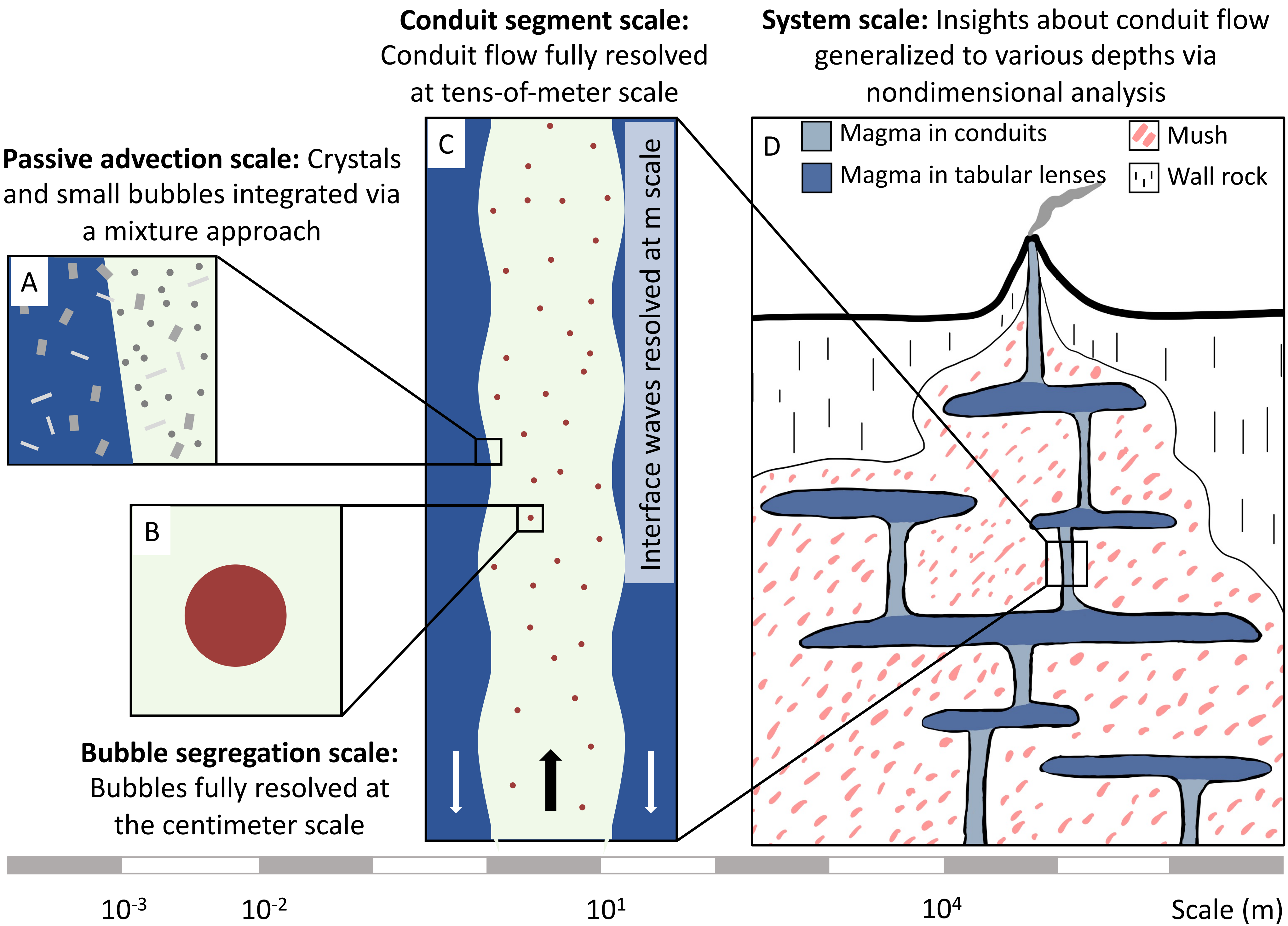

Conduit segment scale:
Conduit flow fully resolved at tens-of-meter scale
System scale: Insights about conduit flow generalized to various depths via nondimensional analysis
Passive advection scale: Crystals and small bubbles integrated via a mixture approach
A
B
C
D
Interface waves resolved at m scale
Magma in conduits
Magma in tabular lenses
Mush
Wall rock
Bubble segregation scale:
Bubbles fully resolved at the centimeter scale
10^{-3}
10^{-2}
10^{1}
10^{4}
Scale (m)

Figure 2.

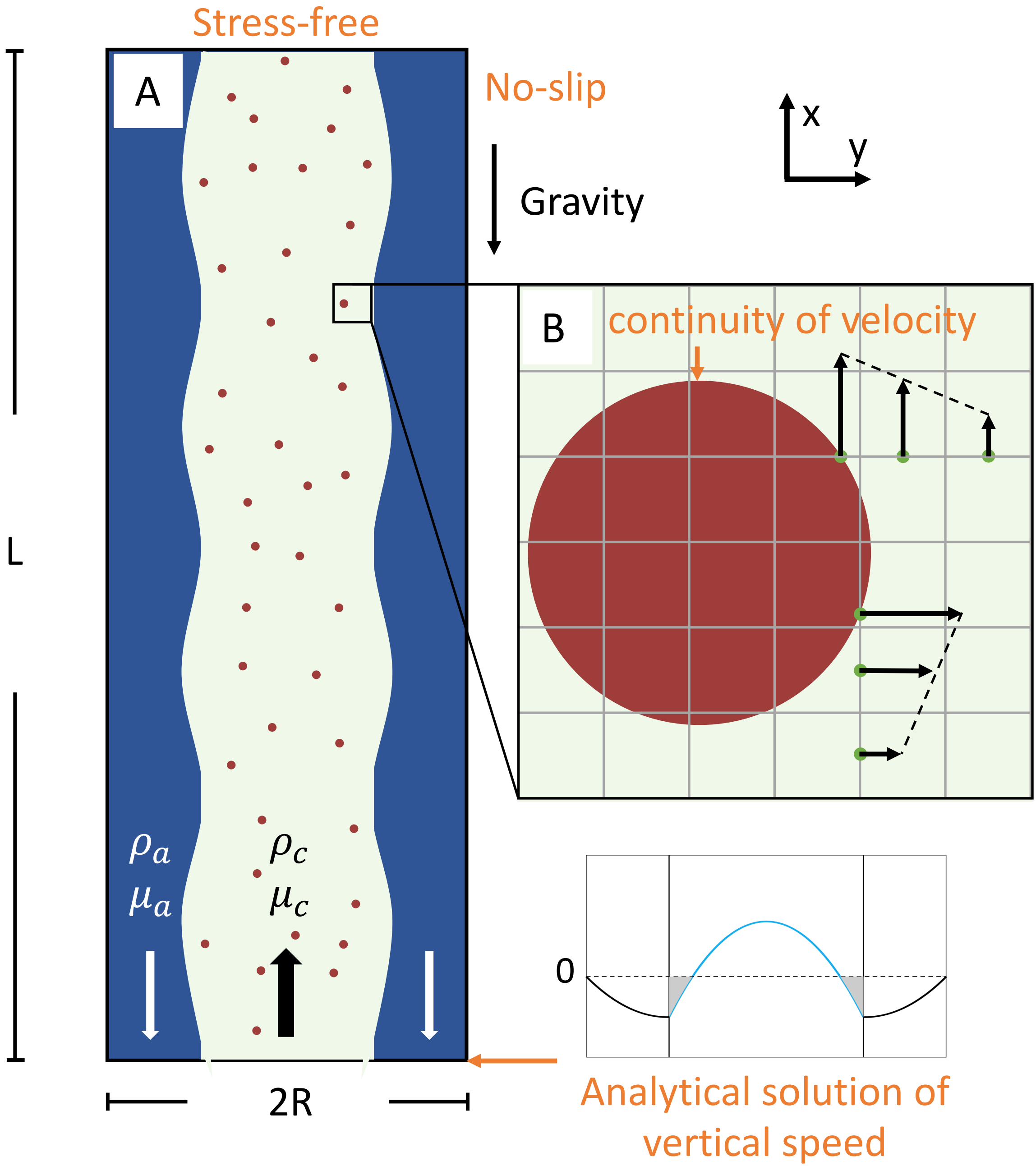

Stress-free
A
No-slip
x
y
Gravity
B
continuity of velocity
L
ρ_a
μ_a
ρ_c
μ_c
0
2R
Analytical solution of vertical speed

Figure 3.

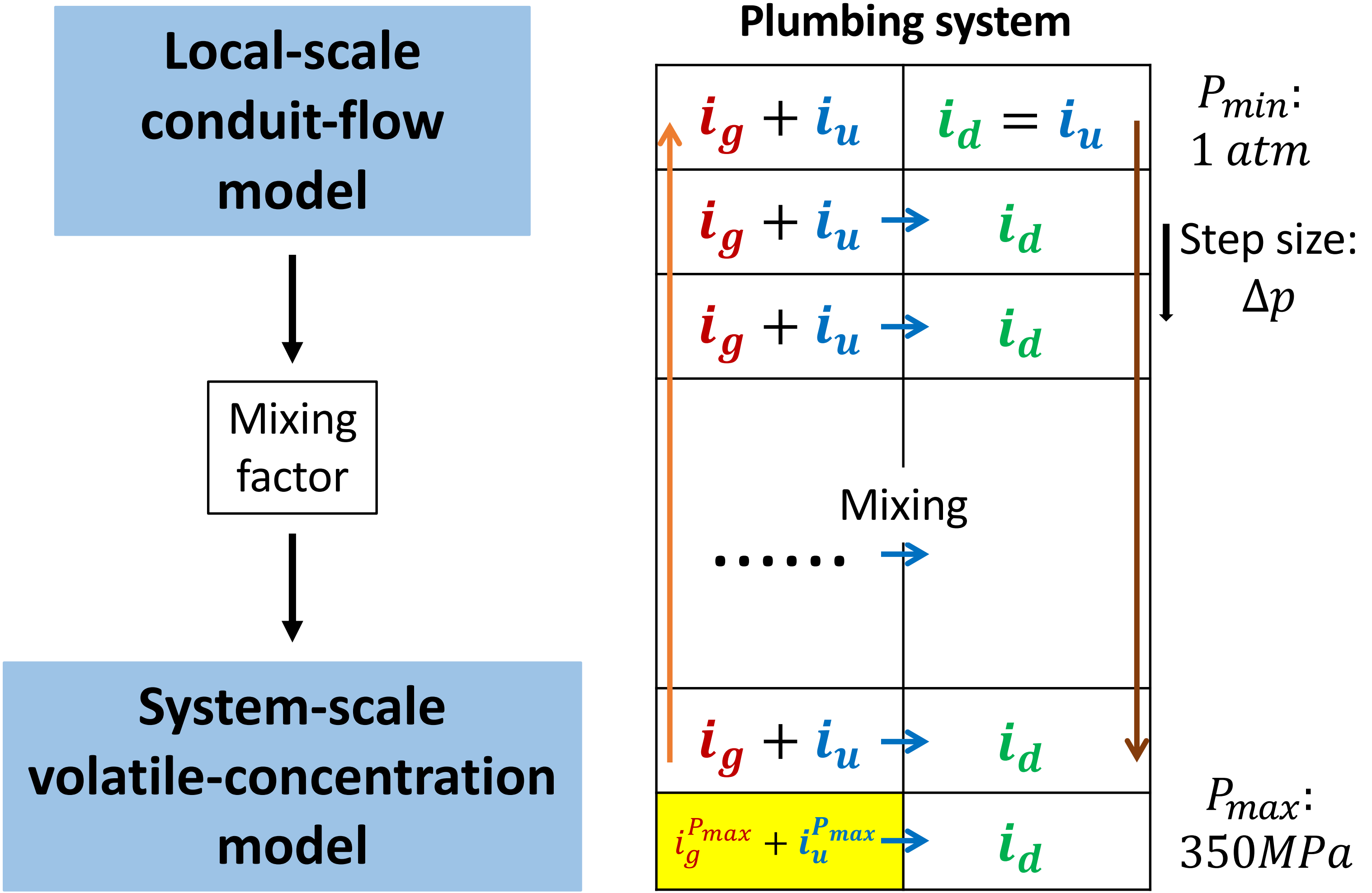

Local-scale conduit-flow model
Mixing factor
System-scale volatile-concentration model
Plumbing system
$i_g + i_u$
$i_d = i_u$
i_d
Mixing
......
$i_g^{P_{max}} + i_u^{P_{max}}$
P_{min}: $1\ atm$
Step size: Δp
P_{max}: $350 MPa$

Figure 4.

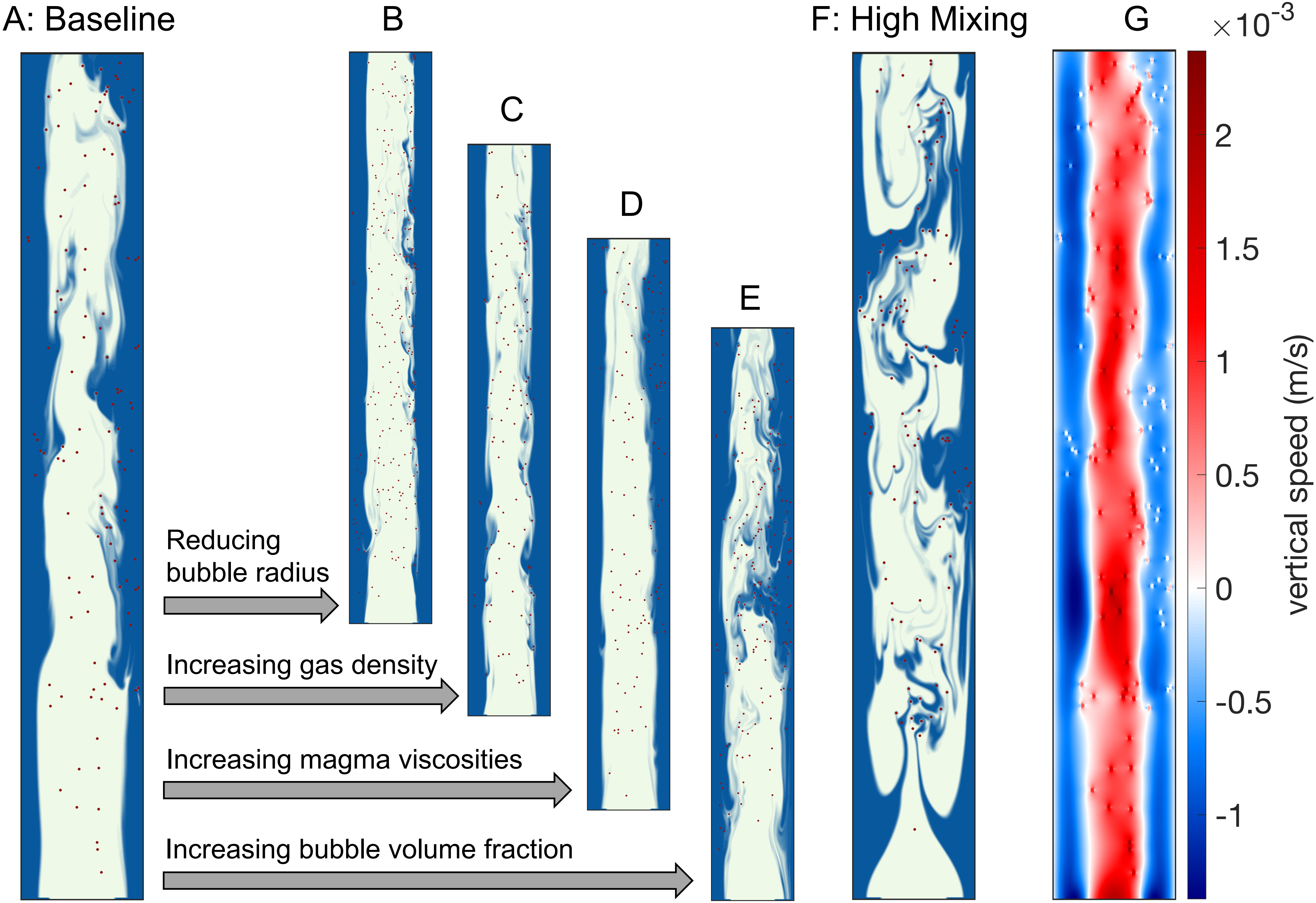
A: Baseline
B
C
D
E
F: High Mixing
G
Reducing bubble radius
Increasing gas density
Increasing magma viscosities
Increasing bubble volume fraction
$\times 10^{-3}$
2
1.5
1
0.5
0
-0.5
-1
vertical speed (m/s)

Figure 5.

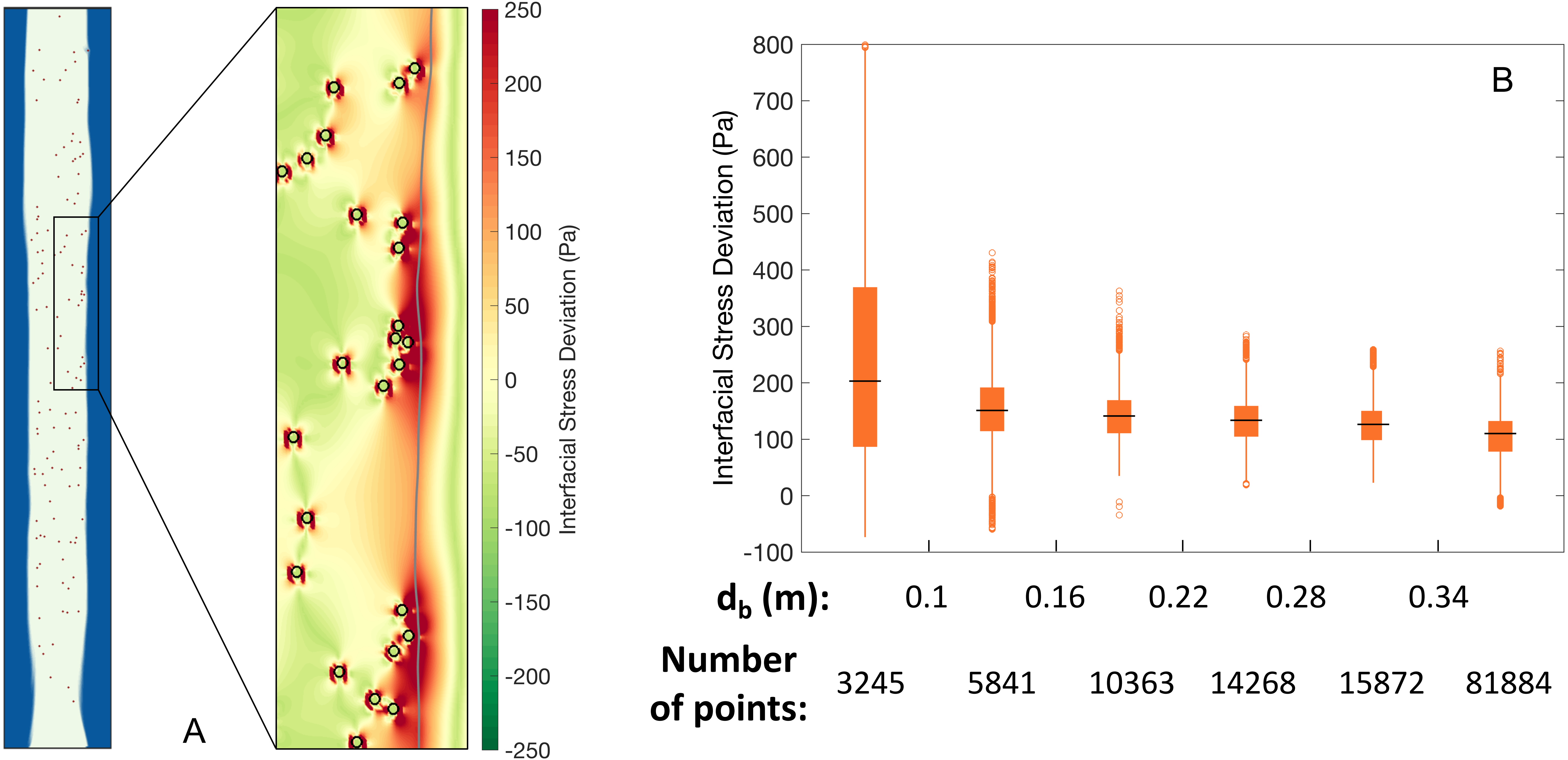

A
250
200
150
100
50
0
-50
-100
-150
-200
-250
Interfacial Stress Deviation (Pa)
B
800
700
600
500
400
300
200
100
0
-100
Interfacial Stress Deviation (Pa)
d_b (m):
0.1
0.16
0.22
0.28
0.34
Number of points:
3245
5841
10363
14268
15872
81884

Figure 6.

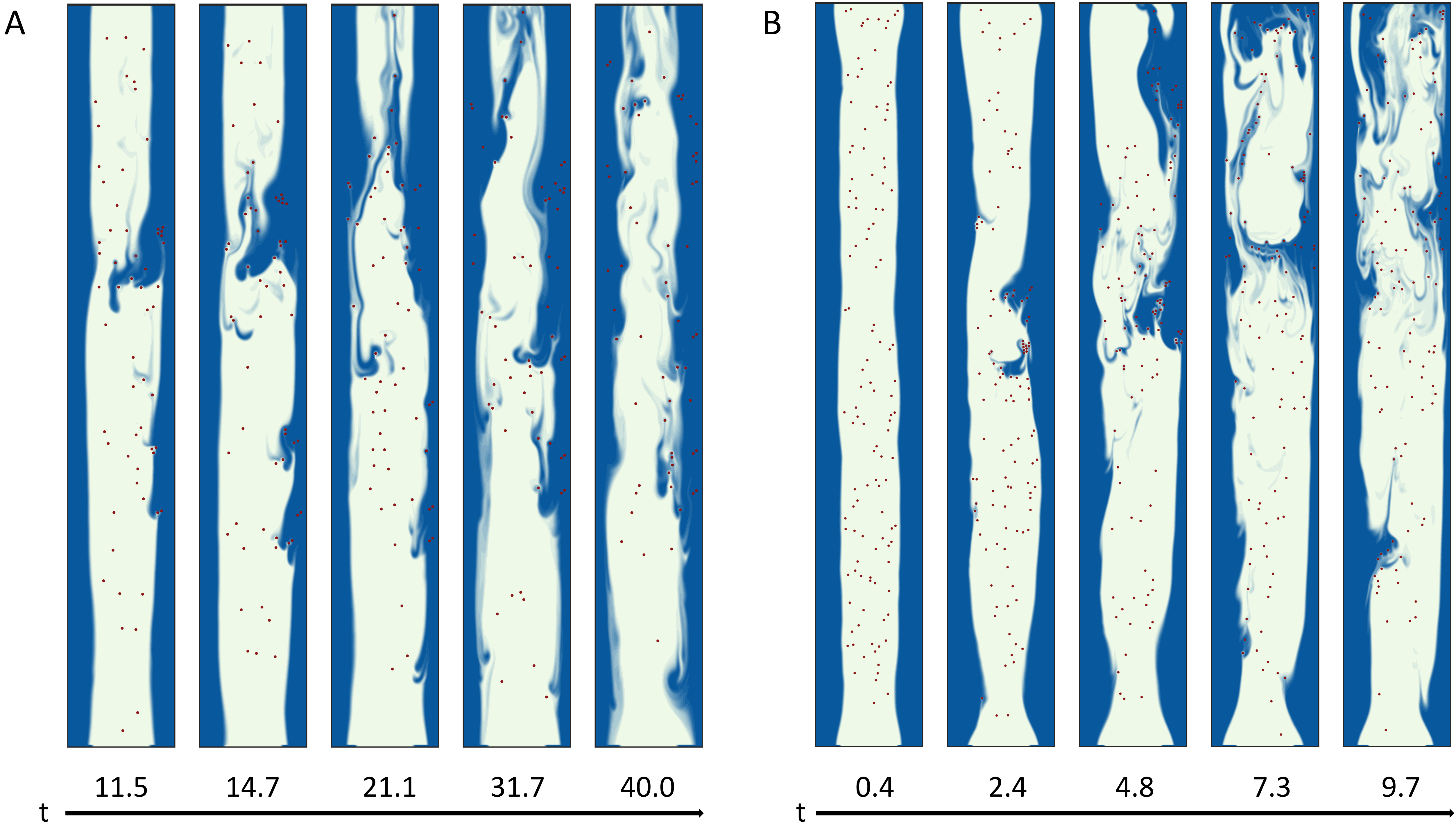
A
B
11.5
14.7
21.1
31.7
40.0
0.4
2.4
4.8
7.3
9.7
t
t

Figure 7.

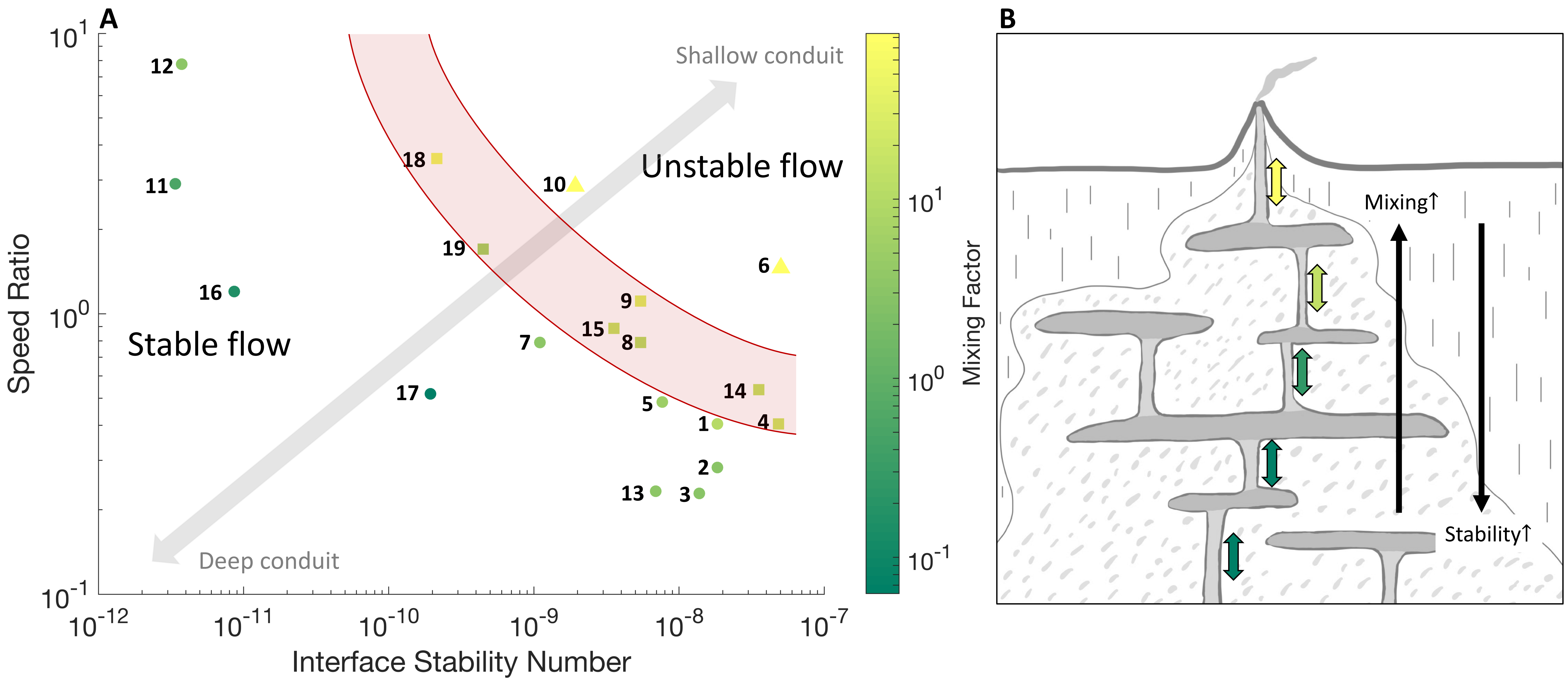
A
B
Shallow conduit
Unstable flow
Stable flow
Deep conduit
Speed Ratio
Interface Stability Number
Mixing Factor
10^{1}
10^{0}
10^{-1}
10^{-12}
10^{-11}
10^{-10}
10^{-9}
10^{-8}
10^{-7}
12
11
16
17
18
10
19
9
15
8
7
5
1
2
13
3
14
4
6
Mixing↑
Stability↑

Figure 8.

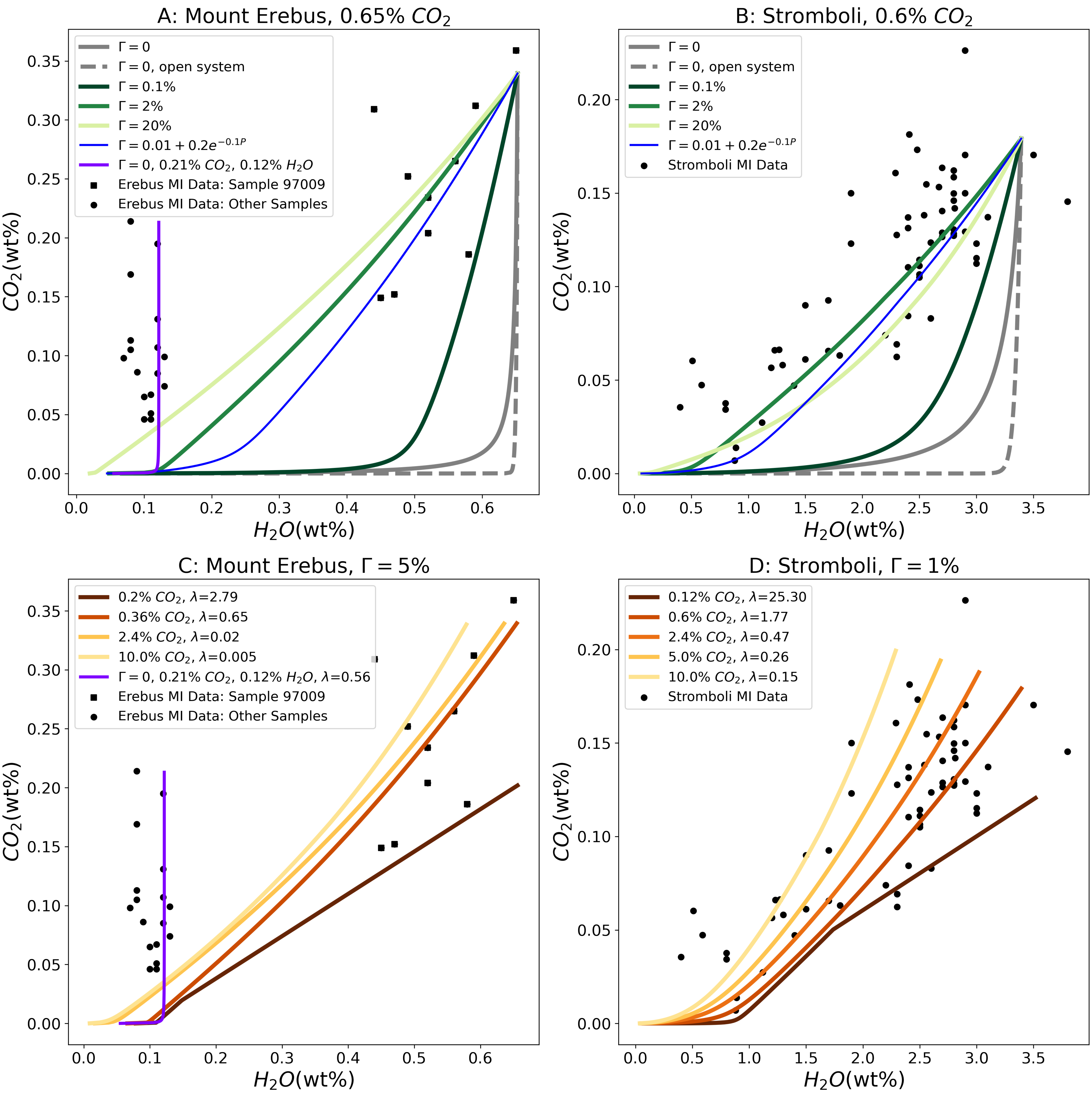

A: Mount Erebus, 0.65% CO_2
$\Gamma = 0$
$\Gamma = 0$, open system
$\Gamma = 0.1\%$
$\Gamma = 2\%$
$\Gamma = 20\%$
$\Gamma = 0.01 + 0.2e^{-0.1P}$
$\Gamma = 0$, 0.21% CO_2, 0.12% H_2O
Erebus MI Data: Sample 97009
Erebus MI Data: Other Samples
CO_2(wt%)
H_2O(wt%)
B: Stromboli, 0.6% CO_2
$\Gamma = 0$
$\Gamma = 0$, open system
$\Gamma = 0.1\%$
$\Gamma = 2\%$
$\Gamma = 20\%$
$\Gamma = 0.01 + 0.2e^{-0.1P}$
Stromboli MI Data
CO_2(wt%)
H_2O(wt%)
C: Mount Erebus, $\Gamma = 5\%$
0.2% CO_2, λ=2.79
0.36% CO_2, λ=0.65
2.4% CO_2, λ=0.02
10.0% CO_2, λ=0.005
$\Gamma = 0$, 0.21% CO_2, 0.12% H_2O, λ=0.56
Erebus MI Data: Sample 97009
Erebus MI Data: Other Samples
CO_2(wt%)
H_2O(wt%)
D: Stromboli, $\Gamma = 1\%$
0.12% CO_2, λ=25.30
0.6% CO_2, λ=1.77
2.4% CO_2, λ=0.47
5.0% CO_2, λ=0.26
10.0% CO_2, λ=0.15
Stromboli MI Data
CO_2(wt%)
H_2O(wt%)